Influence of an intrinsically disordered region on protein domains revealed by NMR-based electrostatic potential measurements

Binhan Yu, Xi Wang, Kyle N. Tan[†], and Junji Iwahara^{*}

Department of Biochemistry and Molecular Biology, Sealy Center for Structural Biology and Molecular Biophysics, University of Texas Medical Branch, Galveston, Texas 77555-1068, USA.

Supporting Information Placeholder

ABSTRACT: Many human proteins possess intrinsically disordered regions containing consecutive aspartate or glutamate residues ('D/E repeats'). Approximately a half of them are DNA/RNA-binding proteins. In this study, using nuclear magnetic resonance (NMR) spectroscopy, we investigated the electrostatic properties of D/E repeats and their influence on folded domains within the same protein. Local electrostatic potentials were directly measured for the HMGB1 protein, its isolated D/E repeats, and the DNA-binding domains by NMR. The data provide quantitative information about the electrostatic interactions between distinct segments of HMGB1. Due to the interactions between the D/E repeats and the DNA-binding domains, local electrostatic potentials of the DNA-binding domains within the fulllength HMGB1 protein were largely negative despite the presence of many positively charged residues. Our NMR data on counterions and electrostatic potentials show that the D/E repeats and DNA have similar electrostatic properties and compete for the DNA-binding domains. The competition promotes dissociation of the protein-DNA complex and influences the molecular behavior of the HMGB1 protein. These effects may be general among the DNA/RNA-binding proteins with D/E repeats.

Hundreds of human proteins have low-complexity sequences of consecutive aspartate (D) or glutamate (E) residues, which are referred to as D/E repeats (examples shown in Figure 1A).^{1,2} Approximately 50% of proteins containing D/E repeats are DNA/RNA-binding proteins. For some of them, the D/E repeats interact with the DNA -binding domains within the same polypeptide chain and association diminish with DNA, the autoinhibition.³⁻⁸ Other D/E repeats can exhibit chaperone-like activity. 9,10 Currently, however, very little is known about the physicochemical properties of D/E repeats. In this paper, using NMR spectroscopy, we demonstrate that D/E repeats have electrostatic properties similar to those of DNA and electrostatically influence the DNA-binding domains via intramolecular interactions, competing with DNA.

We first investigated the electrostatic properties of the 31residue peptide containing D/E repeats of 30 residues that correspond to the C-terminal tail (residues 186-215) of the human HMGB1 protein. We referred to this peptide as DERT30. Figure 1B shows ¹H-¹⁵N heteronuclear HISQC¹¹ and direct ¹³C-detected CON¹² spectra recorded for ¹³C/¹⁵N-labeled DERT30. Despite the low complexity of its sequence, many cross peaks in these spectra were well isolated owing to sharp¹⁵N and ¹³C=O resonances of the IDR. Through direct ¹³C-detected ¹³ and ¹H-detected ¹⁴ NMR experiments, we assigned each isolated signal from the D/E repeats (see Figures S1-S2 and Materials and Methods described in the Supporting Information [SI]). Negative heteronuclear [¹H-]¹⁵N NOE values (Figure 1C) and small ¹⁵N chemical shift anisotropy (CSA) / ¹⁵N-¹H dipole-dipole (DD) cross-correlation rates (Figure S3) for backbone NH groups¹⁵ clearly indicate that D/E repeats are structurally disordered.

Using NMR data of solvent paramagnetic relaxation enhancement (PRE) arising from aminomethyl-PROXYL (charge, +1e) and carbamoyl-PROXYL (neutral) as paramagnetic cosolutes, we measured effective nearsurface electrostatic potentials ϕ_{ENS} around DERT30. Since our group developed the NMR method to measure ϕ_{ENS} potentials in 2021, ¹⁶ we and others have applied it to various biomolecules, as recently reviewed.¹⁷ In the current study, we measured the solvent PRE Γ_2 rates on backbone ${}^{1}\text{H}_{\alpha}$ nuclei (Figure S4) to determine ϕ_{ENS} potentials. We analyzed data for ${}^{1}H_{\alpha}$ nuclei instead of ${}^{1}H_{N}$ nuclei because backbone amide groups of a disordered polypeptide at neutral pH typically undergo rapid hydrogen exchange, 18 which may adversely impact solvent PRE rates (Γ_2). Figure 1D shows the effective near-surface electrostatic potentials ϕ_{ENS} determined from the solvent PRE data. Interestingly, the overall magnitude of the negative potentials for the D/E repeat was even larger than that of potentials previously measured for the 15-bp DNA¹⁹ under the same conditions.

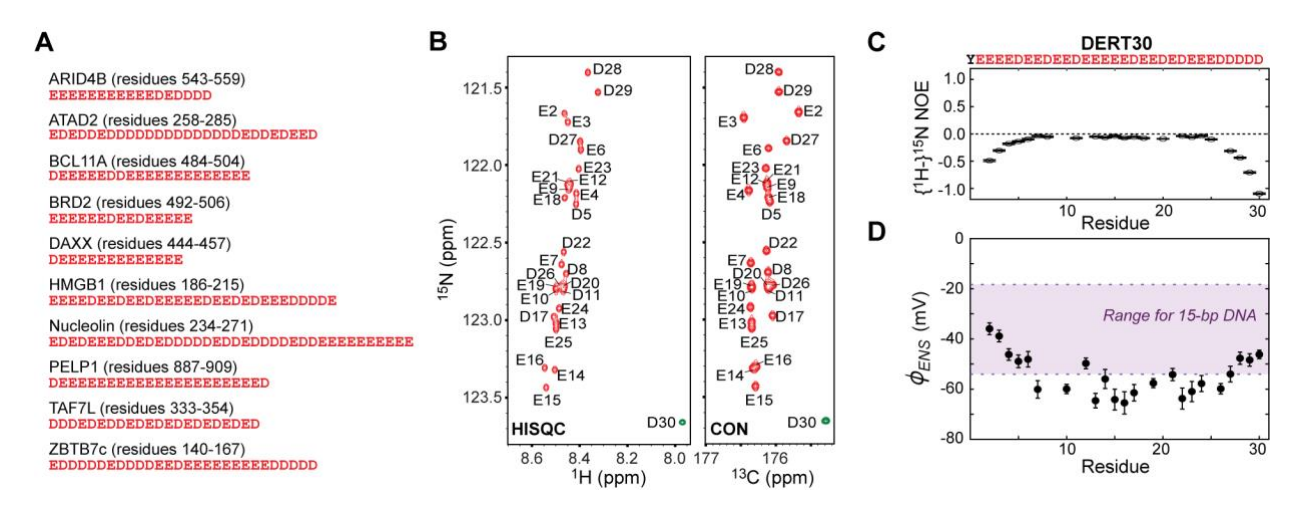


Figure 1. NMR of D/E repeats. (**A**) Examples of D/E repeats in human proteins. A complete list of D/E repeats (10 consecutive residues or longer) in human proteins is given as Table S1. (**B**) 1 H- 15 N HISQC and 13 C-detected CON spectra recorded for 13 C/ 15 N-labeled DERT30 in a buffer of 20 mM Tris•acetate (pH 7.5), 100 mM NaCl, and 5% D₂O at 25°C. Annotations indicate 15 N resonance assignment. (**C**) [1 H-] 15 N heteronuclear NOE²⁰ measured for DERT30 NH groups at the 1 H frequency of 750 MHz. (**D**) Effective near-surface electrostatic potentials ϕ_{ENS} measured using solvent PRE data for 1 H_α nuclei. For comparison, the range of the ϕ_{ENS} potentials that were previously measured for 15-bp DNA¹⁹ are indicated with the purple shade.

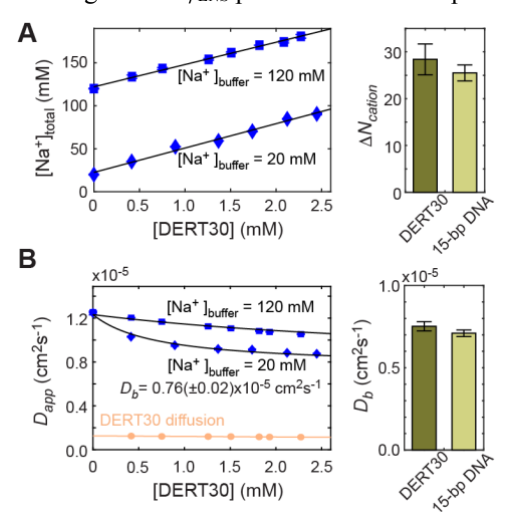


Figure 2. Counterion condensation by the D/E repeats. (A) ²³Na NMR-based ion-counting data. The total concentrations of Na+ ions in DERT30 solutions were measured after equilibration with a buffer of 20 mM HEPES•NaOH (pH 7.5) with (square) and without (diamond) 100 mM NaCl. Due to the cations condensed around the negatively charged macromolecule, the total Na⁺ concentration in the solution is higher than the Na+ concentration in the original buffer, and the slope in the plot corresponds to the number of condensed cations ΔN_{cation} .²¹ (B) Apparent diffusion coefficients of Na⁺ ions at different concentrations of DERT30. The diffusion coefficient for Na⁺ ions condensed around DERT30 (D_b) is also indicated. The diffusion coefficient for DERT30 itself is indicated in orange.

The strong negative electrostatic potentials observed for the D/E repeats reflect their high negative charge density per molecular weight (-0.008*e* per dalton), which is larger than that for DNA (-0.003*e* per dalton). As described in the SI, through computation of Poisson-Boltzmann electrostatic potentials, 22,23 we also predicted ϕ_{ENS} potentials for structural models generated for DERT30 in various conformations: an α -helix, a β -strand, and random coils (Figure S5). The majority of experimental ϕ_{ENS} potentials were within the range of values predicted for various random coil conformations but tended to be close to the largest magnitudes predicted. This may reflect known limitations of the Poisson-Boltzmann theory for highly charged systems. 24,25

For further investigation of the electrostatic properties of D/E repeats, we conducted ²³Na NMR experiments as we previously described for DNA (see the SI for details).²¹ The ²³Na NMR data clearly indicated that D/E repeats condense as many counterions as DNA does (Figure 2A). Our ²³Na diffusion data showed that diffusion of the condensed ions is only moderately slowed down by electrostatic attraction to the macromolecules, making the D_b coefficient far greater than the diffusion coefficient of the macromolecules. Nonetheless, the coefficient D_b for Na⁺ ions condensed around DERT30 was close to that for those condensed around the 15-bp DNA (Figure 2B). These data suggest that D/E repeats and DNA have similar electrostatic properties.

To gain insight into the electrostatic impact of D/E repeats on other regions of HMGB1, we measured effective near-surface electrostatic potentials ϕ_{ENS} for the full-length HMGB1 protein and the $\Delta 30$ variant lacking the D/E repeats. Figure 3 shows ϕ_{ENS} potentials measured for these protein constructs of HMGB1. Due to severe overlapping and broadening of signals (Figure S6), we were unable to measure the ϕ_{ENS} potentials for most residues of the D/E repeats in the full-length HMGB1 protein. Nonetheless, many residues in the folded regions were analyzable. The profiles of ϕ_{ENS} potentials were strikingly different between the full-length HMGB1

protein and the $\Delta 30$ variant lacking the D/E repeats. Most residues of the DNA-binding domains exhibited positive potentials in the $\Delta 30$ variant. By contrast, the presence of the D/E repeats in the full-length protein caused negative ϕ_{ENS} potentials for many residues. These results illuminate the strong electrostatic influence of the D/E repeats on the DNA-binding domains of HMGB1.

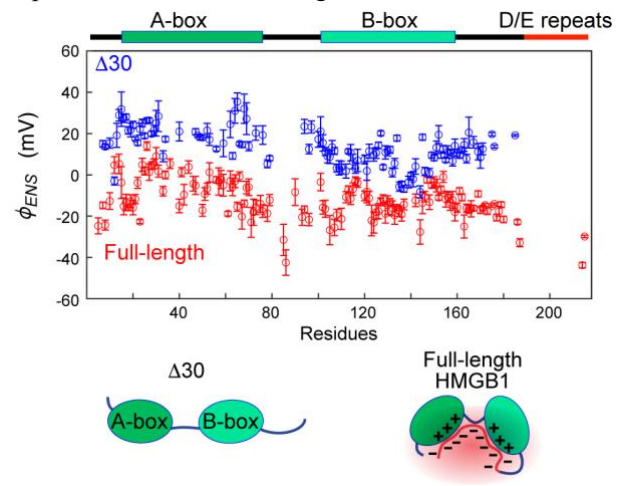


Figure 3. Effective near-surface potentials ϕ_{ENS} measured for the full-length HMGB1 protein (red) and the $\Delta 30$ variant lacking the D/E repeats (blue). Solvent PRE data used to determine the ϕ_{ENS} potentials are shown in Figure S7.

Through NMR experiments, we examined competition between D/E repeats and DNA for the DNA-binding domains. We recorded ¹H-¹⁵N HISQC spectrum for the complex of ¹⁵N-labeled DERT30 and the unlabeled Δ30 variant of HMGB1. Due to the interaction with the DNAbinding domains, the spectrum recorded for the ¹⁵Nlabeled DERT30 was significantly different from the spectrum for the free state, but the signal dispersion remained poor (Figure 4A left). This suggests that the D/E repeats interacting with the $\Delta 30$ variant remain as a random coil, which is also supported by ${}^{13}C_{\alpha}$ chemical shifts (Figure S8). To examine competition between D/E repeats and DNA, we used a four-way junction DNA (32) base pairs) named J1,26 which exhibits high affinities for the full-length HMGB1 8,27 and the $\Delta 30$ variant (the binding affinity data are shown in Figure S9). When unlabeled J1 was added to the solution of the complex of ¹⁵N DERT30 and the unlabeled Δ 30 variant, the signals from ¹⁵N-labeled DERT30 moved toward the chemical shifts for the free state (Figure 4A middle). These NMR data indicate that DNA and the D/E repeats compete for the DNA-binding domains of HMGB1.

The molecular behavior of HMGB1 is significantly influenced by the competition between the D/E repeats and DNA. As shown in Figure 4B, the D/E repeats cause 5-20-fold faster dissociation of HMGB1 from DNA, clearly interfering with the binding of the structured domains with DNA. The $\Delta 30$ variant lacking the D/E repeats exhibited a linear increase of the apparent rate

constant for dissociation (k_{off}^{app}) as a function of the unlabeled DNA concentration. On the contrary, the fulllength HMGB1 protein exhibited a decrease in k_{off}^{app} . Both behaviors can be explained using the kinetic models described in SI Section 3 (see also Figure S12). The linear increase observed for $\Delta 30$ is indicative of the so-called intersegment transfer, whereby a protein transfers from one DNA to another through a transient intermediate bridging two DNA molecules. 28-30 The bridging intermediate can be formed when one of the two DNAbinding domains is dissociated from DNA and captures another DNA molecule. By contrast, the full-length protein did not show any sign of intersegment transfer. As schematically drawn in Figure 4B, the D/E repeats can engage the detached domain (A-box or B-box), thus precluding the formation of the bridging intermediate, and facilitate macroscopic dissociation of the protein from DNA.

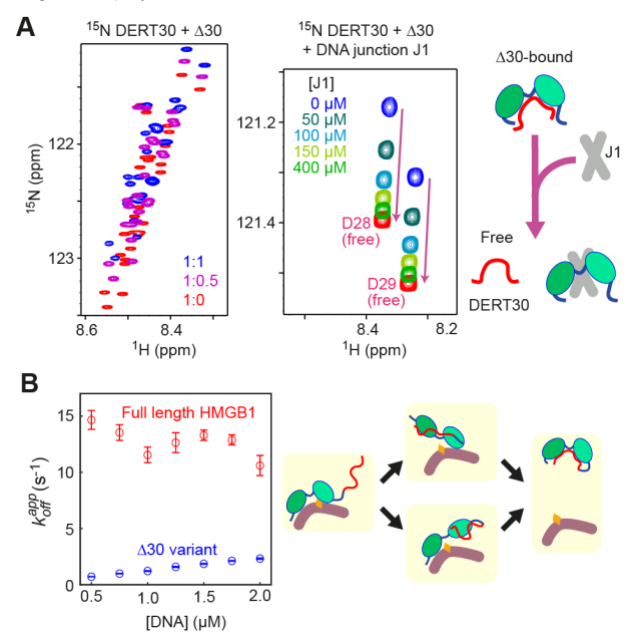


Figure 4. D/E repeats complete with DNA for the DNAbinding domains of HMGB1. (A) Change of ¹H-¹⁵N NMR spectra recorded for ¹⁵N-labeled DERT30. The left panel shows overlaid spectra recorded for $\Delta 30$ -bound (blue) and free (red) states of ¹⁵N DERT30 (0.2 mM). When the fourway junction DNA J1 (32 base pairs) was added to the solution of the DERT30-Δ30 complex, the NMR signals from DERT30 were found to shift toward those from the free state (right panel). Simulations of this effect using the Bloch-McConnell equation are shown in Figure S10. (B) Apparent rate constant for dissociation (k_{off}^{app}) of the full-length HMGB1 or its Δ30 variant protein from cisplatin-modified DNA. They were measured through stopped-flow fluorescence experiments in which the fluorescence anisotropy was monitored immediately after a solution of the complex (10 nM) of the protein and fluorescence-labeled DNA (20 base pairs) containing a site-specific modification by cisplatin was mixed with a solution of the same DNA with no fluorescence label (0.5-2.0 µM) (Figure S11). The theoretical relationship between the apparent and intrinsic

dissociation rate constants are described in the SI (see also Figure S12).

Overall, our data suggest that despite the completely different chemical structures, D/E repeats can serve as DNA mimetic in terms of electrostatics and strongly influence the molecular properties of DNA-binding proteins. Our previous study showed that the intramolecular interactions between D/E repeats and the DNA-binding domains let the protein molecules avoid the distraction of non-target DNA and thereby accelerate the target search process.31 Because D/E repeats are conformationally more flexible than double-stranded DNA, electrostatic repulsive forces from DNA may induce conformational transitions of the proteins from an autoinhibited state to an uninhibited state, allowing the proteins to bind to DNA.31 Through a reverse process, D/E repeats can also promote dissociation of the protein from DNA (Figure 4B). In this manner, D/E repeats can mobilize the protein bound to DNA and facilitate translocation from one site to another.

In conclusion, our current study shows that D/E repeats have DNA-like electrostatic properties and act as DNA mimicry that affects the molecular properties of a DNAbinding protein. The direct measurement of electrostatic potentials by NMR reveals the electrostatic influence of the D/E repeats on the DNA-binding domains. The D/E repeats compete with DNA for the DNA-binding domains and facilitate dissociation of the protein from DNA. A similar mechanism might also work for RNA-binding proteins containing D/E repeats. It is likely that the approach using NMR-based measurement of electrostatic potentials will be useful for characterization of many other proteins containing intrinsically disordered regions (IDRs) and provide quantitative information about electrostatic interactions between IDRs and folded domains.

ASSOCIATED CONTENT

Supporting Information. The Supporting Information is available free of charge on the ACS Publications website.

Materials and Methods; Figures S1-S12; and Table S1 (PDF).

AUTHOR INFORMATION

Corresponding Author

*Junji Iwahara. Email: j.iwahara@utmb.edu

Present Address

[†]K.N.T.: Biomedical Engineering, Johns Hopkins University. 3400 N. Charles Street, Baltimore, Maryland 21218, USA.

ACKNOWLEDGMENT

This work was supported by Grant MCB-2026805 from the National Science Foundation (to J.I.), Grant R35-GM130326 from the National Institutes of Health (to J.I.),

and Grant H-2104-20220331 from the Welch Foundation (to J.I.).

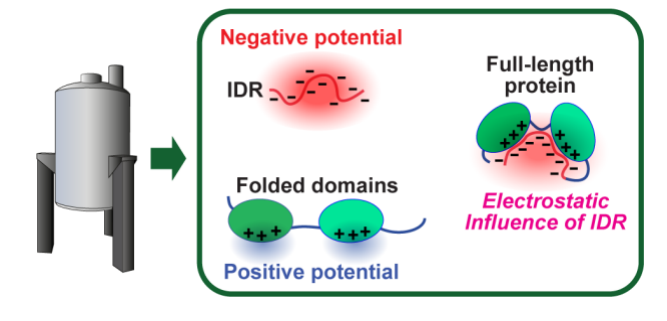
REFERENCES

- (1) Bigman, L. S.; Iwahara, J.; Levy, Y. Negatively Charged Disordered Regions are Prevalent and Functionally Important Across Proteomes. *J Mol Biol* **2022**, *434*, 167660.
- (2) Shukla, S.; Lazarchuk, P.; Pavlova, M. N.; Sidorova, J. M. Genome-wide survey of D/E repeats in human proteins uncovers their instability and aids in identifying their role in the chromatin regulator ATAD2. *iScience* **2022**, *25*, 105464.
- (3) Stott, K.; Watson, M.; Howe, F. S.; Grossmann, J. G.; Thomas, J. O. Tail-mediated collapse of HMGB1 is dynamic and occurs via differential binding of the acidic tail to the A and B domains. *J Mol Biol* **2010**, *403*, 706.
- (4) Watson, M.; Stott, K.; Thomas, J. O. Mapping intramolecular interactions between domains in HMGB1 using a tail-truncation approach. *J Mol Biol* **2007**, *374*, 1286.
- (5) Wiebe, M. S.; Nowling, T. K.; Rizzino, A. Identification of novel domains within Sox-2 and Sox-11 involved in autoinhibition of DNA binding and partnership specificity. *J Biol Chem* **2003**, *278*, 17901.
- (6) Wang, X.; Greenblatt, H. M.; Bigman, L. S.; Yu, B.; Pletka, C. C.; Levy, Y.; Iwahara, J. Dynamic Autoinhibition of the HMGB1 Protein via Electrostatic Fuzzy Interactions of Intrinsically Disordered Regions. *J Mol Biol* **2021**, *433*, 167122.
- (7) Ueshima, S.; Nagata, K.; Okuwaki, M. Internal Associations of the Acidic Region of Upstream Binding Factor Control Its Nucleolar Localization. *Mol Cell Biol* **2017**, *37*, e00218.
- (8) Wang, X.; Mayorga-Flores, M.; Bien, K. G.; Bailey, A. O.; Iwahara, J. DNA-mediated proteolysis by neutrophil elastase enhances binding activities of the HMGB1 protein. *J Biol Chem* **2022**, *298*, 102577
- (9) Huang, L.; Agrawal, T.; Zhu, G.; Yu, S.; Tao, L.; Lin, J.; Marmorstein, R.; Shorter, J.; Yang, X. DAXX represents a new type of protein-folding enabler. *Nature* **2021**, *597*, 132.
- (10) Sitron, C. S.; Hartl, F. U. A new way of D/Ealing with protein misfolding. *Mol Cell* **2021**, *81*, 4114.
- (11) Yuwen, T.; Skrynnikov, N. R. CP-HISQC: a better version of HSQC experiment for intrinsically disordered proteins under physiological conditions. *J Biomol NMR* **2014**, *58*, 175.
- (12) Gil, S.; Hošek, T.; Solyom, Z.; Kümmerle, R.; Brutscher, B.; Pierattelli, R.; Felli, I. C. NMR Spectroscopic Studies of Intrinsically Disordered Proteins at Near-Physiological Conditions. *Angew Chem Int Ed* **2013**, *52*, 11808.
- (13) Felli, I. C.; Pierattelli, R. ¹³C Direct Detected NMR for Challenging Systems. *Chem Rev* **2022**, *122*, 9468.
- (14) Cavanagh, J.; Fairbrother, W. J.; Palmer, A. G., III; Rance, M.; Skelton, N. J. *Protein NMR Sprectroscopy: Principles and Practice*; 2 ed.; Elsevier Academic Press: Burlignton, 2007.
- (15) Palmer, A. G., 3rd NMR probes of molecular dynamics: overview and comparison with other techniques. *Annu Rev Biophys Biomol Struct* **2001**, *30*, 129.
- (16) Yu, B.; Pletka, C. C.; Pettitt, B. M.; Iwahara, J. De novo determination of near-surface electrostatic potentials by NMR. *Proc Natl Acad Sci U S A* **2021**, *118*, e2104020118.
- (17) Iwahara, J.; Pettitt, B. M.; Yu, B. Direct measurements of biomolecular electrostatics through experiments. *Curr Opin Struct Biol* **2023**, *82*, 102680.
- (18) Dyson, H. J.; Wright, P. E. NMR illuminates intrinsic disorder. *Curr Opin Struct Biol* **2021**, *70*, 44.
- (19) Yu, B.; Wang, X.; Iwahara, J. Measuring Local Electrostatic Potentials Around Nucleic Acids by Paramagnetic NMR Spectroscopy. *J Phys Chem Lett* **2022**, *13*, 10025.
- (20) Grzesiek, S.; Bax, A. The importance of not saturating H₂O in protein NMR. Application to sensitivity enhancement and NOE measurements. *J Am Chem Soc* **1993**, *115*, 12593.
- (21) Yu, B.; Bien, K. G.; Pletka, C. C.; Iwahara, J. Dynamics of Cations around DNA and Protein as Revealed by ²³Na Diffusion NMR Spectroscopy. *Anal Chem* **2022**, *94*, 2444.

- (22) Jurrus, E.; Engel, D.; Star, K.; Monson, K.; Brandi, J.; Felberg, L. E.; Brookes, D. H.; Wilson, L.; Chen, J.; Liles, K. *et al.* Improvements to the APBS biomolecular solvation software suite. *Protein Sci* **2018**, *27*, 112.
- (23) Fogolari, F.; Brigo, A.; Molinari, H. The Poisson-Boltzmann equation for biomolecular electrostatics: a tool for structural biology. *J Mol Recognit* **2002**, *15*, 377.
- (24) Grochowski, P.; Trylska, J. Continuum molecular electrostatics, salt effects, and counterion binding—A review of the Poisson–Boltzmann theory and its modifications. *Biopolymers* **2008**, *89*, 93.
- (25) Netz, R. R.; Orland, H. Beyond Poisson-Boltzmann: Fluctuation effects and correlation functions. *Eur Phys J E* **2000**, *1*, 203
- (26) Kallenbach, N. R.; Ma, R.-I.; Seeman, N. C. An immobile nucleic acid junction constructed from oligonucleotides. *Nature* **1983**, 305, 829
- (27) Troisi, M.; Klein, M.; Smith, A. C.; Moorhead, G.; Kebede, Y.; Huang, R.; Parker, E.; Herrada, H.; Wade, E.; Smith, S. et al.

- Conformation and protein interactions of intramolecular DNA and phosphorothioate four-way junctions. *Exp Biol Med (Maywood)* **2021**, 246 707
- (28) Itoh, Y.; Murata, A.; Takahashi, S.; Kamagata, K. Intrinsically disordered domain of tumor suppressor p53 facilitates target search by ultrafast transfer between different DNA strands. *Nucleic Acids Res* **2018**, *46*, 7261.
- (29) Esadze, A.; Iwahara, J. Stopped-flow fluorescence kinetic study of protein sliding and intersegment transfer in the target DNA search process. *J Mol Biol* **2014**, *426*, 230.
- (30) Doucleff, M.; Clore, G. M. Global jumping and domain-specific intersegment transfer between DNA cognate sites of the multidomain transcription factor Oct-1. *Proc Natl Acad Sci U S A* **2008**, *105*, 13871.
- (31) Wang, X.; Bigman, L. S.; Greenblatt, H. M.; Yu, B.; Levy, Y.; Iwahara, J. Negatively charged, intrinsically disordered regions can accelerate target search by DNA-binding proteins. *Nucleic Acids Res* **2023**, *51*, 4701.

TOC graphic



SUPPORTING INFORMATION

Influence of an intrinsically disordered region on protein domains revealed by NMR-based electrostatic potential measurements

Binhan Yu, Xi Wang, Kyle N. Tan, and Junji Iwahara

Department of Biochemistry and Molecular Biology, Sealy Center for Structural Biology and Molecular Biophysics, University of Texas Medical Branch, Galveston, Texas 77555-1068, USA

1. Materials and Methods

Preparation of DERT30

A pET50b-derivative plasmid containing a codon-optimized synthetic gene of the His6tagged SUMO-DERT30 fusion protein at NdeI/PacI sites was purchased from GenScript, Inc. The plasmid was used for transformation of the Escherichia coli strain BL21 (DE3). A transformed clone was cultured at 37°C in a total of 2-L media containing 30 µg/ml kanamycin (as the selection marker), 1 g/L ¹⁵NH₄Cl (as the sole nitrogen source) and 2 g/L ¹³C-glucose (as the sole carbon source). When the optical density at 600 nm reached 0.8, expression of the His6-tagged SUMO-DERT30 fusion protein was induced by adding 0.4 mM isopropyl β-D-1-thiogalactopyranoside (IPTG). Immediately after the addition of IPTG, the culture temperature was changed to 18°C and the culture was continued at this temperature for 16 hours. The cells were harvested through a centrifugation at 4,000 × g and suspended in a ~80 ml buffer of 20 mM Tris•HCl, 1 mM EDTA, 500 mM NaCl, 2 mM dithiothreitol (DTT) and 5% Glycerol at pH 7.5. The buffer also contained a Roche Complete protease inhibitors cocktail (2 tablets per 100 ml). The suspended cells were stored at -70°C until use. For isolation of the His6-tagged SUMO-DERT30 fusion protein, the cells were defrosted and broken by sonication. After centrifugation of the lysate at $30,000 \times g$ for 20 minutes at 4°C, the supernatant was loaded onto a 20-ml His Prep FF column equilibrated with a buffer of 50 mM Tris•HCl, 500 mM NaCl, 5 mM imidazole and 5% Glycerol at pH7.5. The column was washed with 50 ml of a buffer of Tris•HCl, and then, the His6-tagged SUMO-DERT30 fusion protein was eluted by a gradient of 5-400 mM imidazole in a buffer of Tris•HCl. The isolated fusion protein was cleaved by the His6-tagged Ulp1c SUMO protease. To remove the protease and the resultant His₆-SUMO tag, the reaction mixture was passed through a 20-ml His Prep FF column. The flow-through was collected and loaded onto a Resource-Q column equilibrated with a buffer of 50 mM Tris•HCl and 1 mM EDTA at pH7.5. DERT30 was eluted through a gradient of 0-1500 mM NaCl in the same buffer. The peptide was quantified using UV absorbance at 280 nm along with the extinction coefficient of 1,490 M⁻¹ cm⁻¹, which was predicted by the ExPasy ProtParam server (https://web.expasy.org/cgi-bin/protparam).

Preparation of HMGB1 and its $\Delta 30$ variant

¹⁵N-labeled HMGB1 and its Δ30 variant were expressed in Escherichia coli strain BL21 (DE3) and purified using ion-exchange and size-exclusion columns as previously described. The purified

proteins were lyophilized and kept at -20°C until use. The HMGB1 and its $\Delta 30$ variant proteins were quantified using UV absorbance at 280 nm along with an extinction coefficient of 21,555 M⁻¹ cm⁻¹, which was predicted by the ExPasy ProtParam server.

Preparation of DNA

All DNA strands used in the current study were chemically synthesized and were purchased from Integrated DNA Technologies, Inc. The four-way junction DNA J1 was composed of four oligonucleotides designed by Kallenbach et al.²: J1A, CGCAATCCTGAGCACG; J1B, CGTGCTCACCGAATGC; J1C, GCATTCGGACTATGGC; and J1D, GCCATAGTGGATTGCG. The FAM moiety was attached to the 5'-terminus of the J1A strand during DNA synthesis. Each strand was purified using Mono-Q anion exchange chromatography. After annealing of an equimolar mixture of the four strands, the four-way junction J1 was further purified by Mono-Q anion exchange chromatography. The 20-bp DNA with cisplatin modification was prepared as previously described. Briefly, a 20-mer DNA strand containing single GpG site (CTCTGGACCTTCCTTTCT; denoted GG20) was platinated by addition of activated cisplatin solution. The reaction product was purified by Resource-Q anion exchange chromatography. After annealing of complimentary strands, the duplex was further purified by Resource-Q column. For fluorescence studies, FAM was attached to the 5'-terminus of GG20.

¹H/¹³C/¹⁵N NMR resonance assignment

The ¹H, ¹³C, ¹⁵N resonances of the HMGB1 and Δ30 variant proteins under the current experimental conditions were previously assigned.³ The ¹H, ¹³C, and ¹⁵N resonances of DERT30 were assigned using a 520 μl solution of 0.3 mM ¹³C/¹⁵N-labeled DERT30 in a buffer of 100 mM NaCl, 10 mM DMSO, 20 mM Tris•acetate, and 5% D₂O at pH 7.5. An Amicon Ultra-4 device (Millipore) with a molecular weight cut-off at 3 kDa was used for concentrating and buffer equilibration. Although a slight leak of DERT30 was found due to its molecular weight (3.9 kDa) close to the cut-off, the vast majority remained in the upper compartment of the centrifugal filter. For the backbone ¹H/¹³C/¹⁵N resonance assignment, ¹H-¹⁵N HISQC, HNCO, HN(CA)CO, HNCA, HN(CO)CA, HN(COCA)HA, HN(COCA)CB, CON, CO(CA)N, and CA(CO)N spectra were recorded.⁴ In additional to a standard CON spectrum, Asp(D)/Asn(N)-selective and Glu(E)/Gln(O)-selective CON spectra⁵ were also recorded to confirm amino-acid types.⁶ For the direct ¹³C-detected spectra, the virtual ¹³C-¹³C decoupling⁶ was used, and the obtained data were processed with the 'splitcomb' command of Bruker TopSpin software. Because the ¹⁵N chemical shift distribution of the D/E repeats is very narrow, a sufficiently high resolution in the ¹⁵N dimensions was achieved only through a non-constant-time type ¹⁵N chemical shift evolution schemes. To achieve a high resolution in the ${}^{13}C_{\alpha}$ dimension without causing splitting due to ${}^{13}C_{-}$ ¹³C couplings, ¹³C_β-decoupling 180° pulses were used in the ¹³C_α chemical shift evolution schemes. The heteronuclear correlation spectra were recorded at 25°C using Bruker Avance III 800-MHz or 750-MHz spectrometers equipped with a cryogenic TCI probe. NMR data were processed and analyzed with NMR-Pipe⁷ and NMRFAM-SPARKY⁸ programs.

NMR experiments to determine ϕ_{ENS} potentials

Four stock solutions of 1) 60 mM aminomethyl-PROXYL, 20 mM Tris•acetate, 10 mM DMSO, and 5% D₂O at pH 7.5; 2) 50 mM carbamoyl-PROXYL, 20 mM Tris•acetate, 10 mM DMSO, and 5% D₂O at pH 7.5; 3) 60 mM aminomethyl-PROXYL, 10 mM K•HPO₄, 100 mM NaCl, and 5% D₂O at pH 7.4 and 4) 50 mM carboxy-PROXYL, 10 mM K•HPO₄, 100 mM NaCl, and 5% D₂O at pH 7.4 were prepared prior to preparation of the paramagnetic samples of proteins. The concentrations of aminomethyl-PROXYL, carboxy-PROXYL and carbamoyl-PROXYL were measured as previously described. These stock solutions were mixed with a protein solution in the same buffer so that the desired concentration (20 mM) of the paramagnetic cosolute was achieved in the final protein solution without altering the buffer. The paramagnetic samples of DERT30 contained 0.4 mM ¹³C/¹⁵N DERT30, 20 mM Tris•acetate, 100 mM NaCl, 10 mM DMSO, 5% D₂O, and 20 mM aminomethyl-PROXYL or carbamoyl-PROXYL. The paramagnetic samples for the full-length HMGB1 protein or the Δ30 variant contained 0.4 mM ¹⁵N-labeled protein, 10 mM potassium phosphate, 100 mM NaCl, and 5% D₂O at pH 7.4 with 20mM aminomethyl-PROXYL or carboxy-PROXYL, respectively.

A Bruker Avance III 800-MHz spectrometer equipped with a cryogenic TCI cryoprobe was used to measure solvent PRE rates Γ_2 for backbone ¹H nuclei as described previously. ⁹⁻¹⁰ The sample temperature was 25°C. The effective near-surface electrostatic potential ϕ_{ENS} was determined from the PRE data using: ¹¹

$$\phi_{ENS} = \frac{k_B T}{(z_b - z_a)e} \ln \left(\frac{\Gamma_{2,a}}{\Gamma_{2,b}}\right)$$
 [s1],

where $\Gamma_{2,a}$ and $\Gamma_{2,b}$ are the solvent PRE rates for aminomethyl-PROXYL and carbamoyl-PROXYL/carboxy-PROXYL, respectively; z is the valance of electric charge (z=1 for aminomethyl-PROXYL; z=0 for carbamoyl-PROXYL; and z=-1 for carboxy-PROXYL); e is the elementary electric charge; k_B is the Boltzmann constant; and T is temperature. As previously described, the ϕ_{ENS} potentials were determined only for 1 H nuclei that satisfied the following criteria: $\Gamma_{2,a} > 3\sigma_a$; $\Gamma_{2,b} > 3\sigma_b$; and $\Gamma_{2,a} / \Gamma_{2,b} > 3\sigma_{ratio}$, where σ_a , σ_b and σ_{ratio} are the uncertainties in $\Gamma_{2,a}$, $\Gamma_{2,b}$, and $\Gamma_{2,a} / \Gamma_{2,b}$. The uncertainties in ϕ_{ENS} potentials were determined using:

$$\sigma_{\phi} = \frac{k_B T}{|z_b - z_a|e} \sqrt{(\sigma_a/\Gamma_{2,a})^2 + (\sigma_b/\Gamma_{2,b})^2}$$
 [s2].

MATLAB was used to calculate the ϕ_{ENS} potentials and their uncertainties.

Poisson-Boltzmann theory-based prediction for structure models

All model structures of the DERT30 peptide shown in Figure S5 were generated using the Xplor-NIH software.¹² The α -helix structure was generated through simulated annealing using backbone torsion angle restraints of Φ = -60 ± 10° and Ψ = -50 ± 10° (through the 'CDIH' potential) and backbone hydrogen bond geometry restraints (through the 'HBDA' and 'HBDB' potentials¹³⁻¹⁴) under the influence of the conformational database potential¹⁵. The extended β -strand was generated through simulated annealing using torsion angle restraints of Φ = -140 ± 1° and Ψ = 130

 \pm 1° for backbone together under the influence of conformational database potentials. A total of 200 random coil structures were generated through simulated annealing with a restraint on the radius of gyration $(R_{gyr})^{16}$ under the influence of the conformational database potential. An ensemble of 100 structures was generated using the setting of R_{gyr} = 15.0 Å, which is based on the empirical equation of Kohn et al. for random coils.¹⁷ Another ensemble of 100 structures was generated using R_{gyr} = 20.0 Å based on speculation that electrostatic repulsion between negatively charged side chains may significantly increase the radius of gyration. For each generated structure model, a PQR-format¹⁸ file containing the coordinates, the charge and the radius for each atom was created using a PDB2PQR program¹⁹. The charge and radius parameters of the AMBER force field were used. Nonlinear Poisson-Boltzmann equation-based electrostatic potentials at the ionic strength of 130 mM were computed for 3D lattice space with a grid interval of 0.5 Å using the APBS software²⁰. The effective near-surface electrostatic potential was predicted using;⁹⁻¹¹

$$\phi_{ENS}^{PB} = \frac{k_B T}{(z_b - z_a)e} \ln \left(\sum_{i} \rho_i r_i^{-6} \exp[-\frac{z_a e \phi_i}{k_B T}] / \sum_{i} \rho_i r_i^{-6} \exp[-\frac{z_b e \phi_i}{k_B T}] \right)$$
 [s3],

in which ϕ_i is the Poisson-Boltzmann electrostatic potential at the grid point i; r_i is the distance from the ¹H nucleus to the grid point i; and ρ_i is a factor that represents the accessibility of the grid point i and is either 1 (accessible) or 0 (inaccessible).

²³Na NMR-based quantification of counterions condensed around DERT30

Ion-counting methods with buffer equilibration were originally developed by Herschlag and coworkers for quantification of counterions around nuclei acids using atomic emission spectroscopy²¹⁻²³ and inductively coupled plasma mass spectrometry²⁴⁻²⁶. Recently, our group adopted the ion-counting methods for NMR spectroscopy and applied to ⁷Li⁺, ²³Na⁺, ¹³³Cs⁺, ¹⁵NH₄⁺, and ¹³C acetate ions around biomolecules.²⁷⁻³⁰ We used ²³Na NMR in the current study. To obtain the data on Na⁺ ions shown in Figure 2A, the DERT30 solutions were equilibrated with a buffer at pH 7.5 containing 20 mM Na⁺. This buffer, which contains Na⁺ as the sole cation, was prepared using 20 mM NaOH titrated with HEPES to adjust pH to 7.5. This buffer preparation method was chosen to avoid any additional cations that would interfere with our NMR-based ion-counting experiments. The buffer equilibration was conducted using Amicon Ultra-4 centrifugal filters (molecular weight cutoff at 3 kDa) until the overall dilution factor exceeds 10,000. ²³Na NMR experiments were conducted at 25°C using a Bruker Avance III spectrometer with an Oxford 17.6-T magnet, where ¹H and ²³Na resonance frequencies are 750 and 198 MHz, respectively, using a DiffBB probe of the broadband observation (BBO) configuration. In each NMR experiment, a coaxial NMR tube was used. The outer tube was a standard 5-mm NMR tube (Norell, Part# S-5-600-7) and the inner tube was a coaxial 2-mm stem insert (Norell, Part# NI5CCI-B). The outer tube contained a 380-µl DERT30 solution, whereas the inner tube contained a reference solution. The reference solution for the ²³Na NMR experiments was 300 mM NaOH, 20% H₂SO₄, and 80% D₂O. The reference solution was designed to produce a ²³Na⁺ NMR signal at a position different from the position of the NMR signal from the cations in the DERT30 solution. ²³Na chemical shifts were referenced to the ²³Na signal from the reference solution in the coaxial inner tube (-1.857

ppm with respect to 0.1 M NaCl in D₂O). The intensity ratio for the two signals was used to quantify cations in the solutions in the outer tube (see below). Another advantage of the use of coaxial tubes is that the annular geometry of the outer-tube liquid suppresses convection that may adversely impact diffusion measurements.³¹

The total concentration of Na⁺ ions ([Na⁺]_{total}), including those in the free and DERT30-bound states, in each DERT30 solution after buffer equilibration was determined from the ratio of the integral of the 23 Na NMR signal from the DERT30 solution to the integral of that from the reference solution ($r = I/I_{ref}$). The Na⁺ concentration in each sample was calculated as [Na⁺]_{buffer} × r_{sample} / r_{buffer} , where [Na⁺]_{buffer} is the Na⁺ concentration in the buffer (i.e., 20 mM) used for the equilibration process; r_{sample} is the integral ratio for the DERT30 solution sample; and r_{buffer} is the integral ratio for the buffer. Because variations in thickness of the coaxial stem-insert glass wall can cause variation in the reference intensity, an identical coaxial stem-insert containing the reference solution was used for all samples of the same series. The dependence of [M⁺]_{total} on the DERT30 concentration (C_D) was analyzed using:²⁸

$$[Na^+]_{total} = [Na^+]_{buffer} + aC_D$$
 [s4].

In Eq. s4, the parameter a corresponds to the ion excess ΔN_{cation} in the main text and was determined as the slope in the linear regression for the C_D -dependent [Na⁺]_{total} data (Figure 2A).

²³Na diffusion experiments

We conducted 23 Na diffusion NMR experiments as described in our previous study on Na⁺ ions around DNA. To obtain the Na⁺ diffusion data shown in Figure 2B, the stimulated echo with bipolar pulsed-gradient pair-longitudinal Eddy-current delay (BPP-LED) pulse sequence³² was applied to 23 Na nuclei using Bruker's standard pulse program ('stebpgp1s'). In the 23 Na diffusion NMR experiment, the magnetic field gradients were varied with 11 different strengths (i.e., 13.6, 38.0, 62.4, 86.9, 111.3, 135.7, 160.1, 184.6, 209.0, 233.5, and 257.9 gauss/cm). The self-diffusion coefficient of liquid N,N-dimethylformamide at 25°C was used to calibrate the pulsed field gradient (PFG) strengths.³³ Each PFG in the BPP schemes was 1.0 ms. The delay Δ between the beginnings of the first and second BPP schemes was 20 ms in the 23 Na diffusion measurements. To determine the apparent diffusion coefficient D for each sample, the following equation was used for nonlinear least-squares fitting for the signal intensity I:³⁴

$$I = I_0 \exp\left[-D\gamma^2 g^2 \delta^2 \left(\Delta - \frac{\delta}{3} - \frac{\tau}{2}\right)\right]$$
 [s5],

in which γ , the ²³Na nuclear gyromagnetic ratio; g, the PFG strength; δ , the total length of a pair of bipolar PFGs; and τ , the time between two gradients in each spin echo. The ²³Na BPP-LED data were processed and analyzed using Bruker TopSpin software.

The apparent diffusion coefficient (D_{app}) of Na⁺ ions was measured for the solutions of DERT30 at varied concentrations. The following equation for fast exchange systems²⁷ was used to analyze the D_{app} data:²⁸

$$D_{app} = p_f D_f + p_b D_b = D_f + (D_b - D_f) a C_D / ([Na^+]_{buffer} + a C_D)$$
[s6],

where D_f and D_b are the diffusion coefficients for cations in the free state and those within the ion atmosphere, respectively. The parameter a in Eq. s6 is identical to that in Eq. s4 and was experimentally determined. The diffusion coefficient D_b for cations within the ion atmosphere was determined from the D_{app} coefficients through nonlinear least-squares fitting with Eq. s6 using the MATLAB software.

Measurement of binding affinity for four-way junction DNA

The binding affinity of the HMGB1 $\Delta 30$ variant protein for the four-way junction DNA J1 was measured using fluorescence-labeled J1 in which one of the four strands was labeled with fluorescein amidite (FAM). FAM fluorescence anisotropy was measured with an ISS PC-1 spectrofluorometer using an excitation wavelength of 490 nm and an emission wavelength of 521 nm at 25°C. The binding assays for FAM-labeled four-way junction was conducted in a buffer of 10mM potassium phosphate (pH 7.4) and 150 mM NaCl. The concentration of FAM-labeled DNA was 4 nM. The dissociation constant K_d was determined from the anisotropy data using MATLAB (MathWorks, Inc), as previously described 35 . The binding affinity of full-length HMGB1 for the four-way junction DNA J1 was previously measured under the same conditions. The measurements of each dissociation constant K_d were triplicated.

Stopped-flow kinetic experiments on dissociation of protein from DNA

The dissociation kinetics were measured for the complexes with cisplatin-modified 20-bp DNA at 25°C using an Applied Photophysics SX20-LED stopped-flow spectrofluorometer. A polarized LED light with maximum intensity at 470 nm was used for excitation of the FAM fluorophore. The fluorescence anisotropy was measured in a real-time manner using two emission channels placed in a T-format configuration with a polarizer and a long-pass filter with a cutoff at 515 nm for each. For each kinetic measurement, the following two solutions were rapidly mixed in a 1:1 volume ratio (80 µl each) by the stopped-flow device: 1) a solution of a complex formed with 50 nM protein (either full-length HMGB1 or Δ30) and 10 nM FAM-labeled 20-bp DNA containing a cisplatin modification; and 2) a solution of varied concentrations (500-2000 nM) of the 20-bp cisplatin-modified DNA with no FAM label. Both solutions were in a buffer containing 10 mM potassium phosphate (pH 7.4) and 100 mM NaCl. Immediately after the flow for mixing had been stopped, the time course data of fluorescence anisotropy were collected for a period of up to 30 s with time intervals ranging from 0.001-0.01 s. For each condition, the measurement was replicated 8-10 times. The obtained anisotropy decay curves were fitted with a single-exponential function. The apparent dissociation rate constants obtained by the fitting were plotted against the concentration of unlabeled competitor DNA and fitted with a linear function. The slope corresponds to the rate constant for intersegment transfer.

2. Bloch-McConnell equation-based simulations of NMR experiments on ^{15}N DERT30 competing with DNA J1 for the $\Delta30$ variant of HMGB1

The system of 15 N-labeled DERT30 in the presence of the $\Delta 30$ variant of HMGB1 (unlabeled) and DNA J1 (unlabeled) can be represented by the following scheme:

$$A + L \Leftrightarrow AL$$
 [s7]

$$B + L \Leftrightarrow BL$$
 [s8]

where the molecules A and B compete for the ligand L, corresponding to DERT30, J1, and the Δ 30, respectively. The equilibrium concentrations [A], [B], [L], [AL], and [BL] can be calculated from the total concentrations (A_{tot} , B_{tot} , and L_{tot}) and the dissociation constants ($K_{d,A}$ and $K_{d,B}$) by solving the following simultaneous equations.

$$[A] + [AL] = A_{tot}$$
 [s9]

$$[B] + [BL] = B_{tot}$$
 [s10]

$$[L] + [AL] + [BL] = L_{tot}$$
 [s11]

[A][L]/[AL] =
$$K_{d,A} = k_{off,A}/k_{on,A}$$
 [s12]

[B][L]/[BL] =
$$K_{d,B} = k_{off,B}/k_{on,B}$$
 [s13]

In Eqs. s12 and s13, k_{on} and k_{off} represent a second-order association rate constant and a first-order dissociation rate constant, respectively. The behavior of transverse magnetization of A can be described by the following Bloch-McConnell equation:

$$\frac{d}{dt}\mathbf{m} = (\mathbf{K} - \mathbf{R} + i\mathbf{W})\mathbf{m}$$
 [s14],

where **m** is a two-dimensional column vector with each element representing magnetization in a form of m_x+im_y for A and AL (i.e., free ¹⁵N DERT30 and ligand-bound ¹⁵N DERT30); **K** is a kinetic matrix; **R** is a relaxation matrix; and **W** is a chemical shift matrix, and *i* is the imaginary number. The matrices are given by:

$$\mathbf{K} = \begin{bmatrix} -k_{on,A}[L] & k_{off,A} \\ k_{on,A}[L] & -k_{off,A} \end{bmatrix}$$
 [s15]

$$\mathbf{R} = \begin{bmatrix} R_{2,A} & 0\\ 0 & R_{2,AL} \end{bmatrix}$$
 [s16]

$$\mathbf{W} = \begin{bmatrix} \Omega_A & 0 \\ 0 & \Omega_{AL} \end{bmatrix}$$
 [s17]

The solution of Eq. s14 is given by:

$$\mathbf{m}(t) = \exp[(\mathbf{K} - \mathbf{R} + i\mathbf{W})t]\mathbf{m}(0)$$
 [s18]

Fourier transformation of the sum of $\mathbf{m}(t)$ elements into a frequency domain gives an NMR spectrum.

Using Eq. s9-s18, we simulated ^{15}N NMR spectra for ^{15}N DERT30 as a function of the concentration of DNA J1 (which corresponds to B_{tot} in Eq. s10). The simulated spectra are shown in Figure S10.

3. Rate equation-based simulations of kinetic experiments shown in Figure 4B

System involving dissociation and association processes

In the stopped-flow experiments shown in Figure 4B, the system involves a protein (P), fluorescence-labeled DNA (D_a), and unlabeled DNA (D_b). The dissociation kinetics was analyzed by monitoring fluorescence immediately after a solution of P and D_a , in which D_a is predominantly in a bound state (PD_a), was mixed with a high-concentration solution of D_b (Figure S11). The protein transfers from D_a to D_b through dissociation (PD_a \rightarrow P + D_a) and association (P + D_b \rightarrow PD_b). The rate equations for this system are given as follows:

$$\frac{d}{dt}[P] = -k_{on}[P]([D_a] + [D_b]) + k_{off}([PD_a] + [PD_b])$$
 [s19]

$$\frac{d}{dt}[D_a] = -k_{on}[P][D_a] + k_{off}[PD_a]$$
 [s20]

$$\frac{d}{dt}[D_b] = -k_{on}[P][D_b] + k_{off}[PD_b]$$
 [s21]

$$\frac{d}{dt}[PD_a] = k_{on}[P][D_a] - k_{off}[PD_a]$$
 [s22]

$$\frac{d}{dt}[PD_b] = k_{on}[P][D_b] - k_{off}[PD_b]$$
 [s23]

An approximate analytical expression is useful to illustrate the meaning of the apparent rate constant from the stopped-flow experiment. Under the condition of $[D_a]_{total} \ll [P]_{total} \ll [D_b]_{total}$, which is the case in our experiments for Figure 4B, the molecular processes involving [P], $[D_b]$, and $[PD_b]$ reach quasi-equilibrium before the system reaches the true equilibrium for all species. Using $k' = k_{on}[P]$, which is approximately constant due to this quasi-equilibrium, Eqs. s20 and s22 can be approximated with:

$$\frac{d}{dt}[D_a] = -k'[D_a] + k_{off}[PD_a]$$
 [s20']

$$\frac{d}{dt}[PD_a] = k'[D_a] - k_{off}[PD_a]$$
 [s22']

This approximation leads to:

$$[D_{a}](t) = \frac{D_{a,tot}k_{off}}{k_{off}+k'} - \left(\frac{D_{a,tot}k_{off}}{k_{off}+k'} - [D_{a}](0)\right) \exp\left[-(k_{off}+k')t\right]$$
[s24]

$$[PD_{a}](t) = \frac{D_{a,tot}k'}{k_{off}+k'} + \left(\frac{D_{a,tot}k_{off}}{k_{off}+k'} - [D_{a}](0)\right) \exp\left[-\left(k_{off} + k'\right)t\right]$$
[s25],

where $D_{a,tot}$ is the total concentration of D_a (i.e., $[D_a] + [PD_a]$). Since Eqs. s24 and s25 share the same exponential term, the time course of the ensemble average of fluorescence $\langle F(t) \rangle$ from D_a and PD_a in the stopped-flow fluorescence experiment will be in a form of:

$$\langle F(t) \rangle = A + B \exp[-k_{off}^{app} t]$$
 [s26],

where the apparent rate constant k_{off}^{app} is given by:

$$k_{off}^{app} = k_{off} + k' = k_{off} \left(1 + P_q / K_d \right) = k_{off} \left(1 + \frac{P_{tot}}{K_d + D_{htot}} \right)$$
 [s27].

In Eq. s27, P_{tot} is the total protein concentration; $D_{b,tot}$ is the total concentration of D_b ; and P_q is [P] at the quasi-equilibrium and is given by $P_q = P_{tot}K_d/(K_d + D_{b,tot})$. When the second term of Eq. s27 is not negligible, k_{off}^{app} will decrease towards k_{off} upon an increase in $D_{b,tot}$ (see Figure S12A).

System involving dissociation, association, and intersegment transfer processes

Some proteins can directly transfer from PD_a to PD_b through a process called intersegment transfer.³⁶⁻³⁸ In this process, a protein molecule transiently bridges two DNA molecules and transfers from one DNA to another without going through the intermediary of the free protein. Phenomenologically, intersegment transfer can be regarded as a second-order process involving a collision between a protein-DNA complex and free DNA.^{37,39} When this additional second-order process is present, the rate equations Eq. s19-s23 should be modified as follows.

$$\frac{d}{dt}[P] = -k_{on}[P]([D_a] + [D_b]) + k_{off}([PD_a] + [PD_b])$$
 [s28]

$$\frac{d}{dt}[D_a] = -(k_{on}[P] + k_{it}[PD_b])[D_a] + (k_{off} + k_{it}[D_b])[PD_a]$$
 [s29]

$$\frac{d}{dt}[D_{b}] = -(k_{on}[P] + k_{it}[PD_{a}])[D_{b}] + (k_{off} + k_{it}[D_{a}])[PD_{b}]$$
 [s30]

$$\frac{d}{dt}[PD_a] = (k_{on}[P] + k_{it}[PD_b])[D_a] - (k_{off} + k_{it}[D_b])[PD_a]$$
 [s31]

$$\frac{d}{dt}[PD_b] = (k_{on}[P] + k_{it}[PD_a])[D_b] - (k_{off} + k_{it}[D_a])[PD_b]$$
 [s32],

where k_{it} is the second-order rate constant for intersegment transfer. As described above, under the condition of $[D_a]_{total} \ll [P]_{total}$, the molecular processes involving [P], $[D_b]$, and $[PD_b]$ reach quasi-equilibrium before the system reaches the true equilibrium for all species. Thus, pseudo-first order approximation is applicable to Eqs. s29 and s31. As shown for Eqs. s20 and s22, the pseudo-first order approximation leads to an exponential function of $\ll F(t)$ in the form of Eq. s26, where the apparent rate constant k_{off}^{app} is given by:

$$k_{off}^{app} = k_{off} \left(1 + \frac{P_{tot}}{K_d + D_{b,tot}} \right) + k_{it} D_{b,tot}$$
 [s33].

When $k_{off} \ll k_{it}D_{b,tot}$, the apparent rate constant k_{off}^{app} becomes a linear increasing function of $D_{b,tot}$ as seen for the data on the $\Delta 30$ variant of HMGB1 in Figure 4B (see also Figure S12B).

Table S1. D/E repeats of 10 or more consecutive aspartate (D) or glutamate (E) residues in human proteins. DNA-binding or RNA-binding proteins (according to Gene Ontology annotations) are indicated in bold. The information was obtained from the UniProt database (https://www.uniprot.org/).

Proteins		D/E repeats (residue numbers)
ABCC9	951	EDEDEEEEEEDEDD 965
ACIN1	270	EEEEEEEEEEDDEEEE 287
ADRA2B	298	EEEEEEEEEE 309
AEBP2	37	EEEEEEEEE 48
AEBP2		EDEDEEEDDEEEEDE 109
Afadin	1577	DEDDEEEEDDD 1587
ALMS1	13	EEEEEEEEEEE 28
AMER1	376	DDDDEEEEEEE 387
ANAPC15	63	DDEEEEDDEDDED 75
ANKRD17	117	EEEEDDDDEEEE 128
ANKRD40	96	EEEDDDDDDDD 106
Anoctamin-8	582	EEDEDDEEEEDEEE 601
ANP32A		DDEEEDEDEEE 178
ANP32A	187	EDEEDEDEEEE 197
ANP32B	175	EDEEDEDDED 184
ANP32B		DEEDEDEDEEEEE 233
ANP32E		EEEEEEEEEDEDEDEDE 204
APBB1		EEEEEDDDDEEEEED 172
APLP2	215	EEEEEDEEEEDEED 232
ARID1B		DDDEEDEEDE 1738
ARID3A		EDEEEEEDEE 157
ARID4B		EEEEEEEDDE 288
ARID4B		EEEEEEEEEDDDDD 559
ARIH1		EEEEDEDDDE 34
ARIH2		EEEEEEEDD 31
ARMC9		DDDEDEDDEED 593
ARMH4		EDEDEEDEEDEEEDEEDEED 637
ARX		EDEEDEDEEEE 242
ASCC2		EEDDDDEEDD 667
Asporin		DDDDDDDDDDDD 51
ATAD2		EDEDDEDDDDDDDDDDDDDDDDDEDEED 285
Atherin		EEEEDDDEDEDDD 343
ATRX		EEEEEEEEED 1997
BAHCC1 BAZ1B		EEEEDEEEEED 1887 DEEEEEEEEEED 1274
BAZ2B		EDEEEDDEEEDEEDDE 627
BBX		EEEEEEDEEED 51
BCL11A		DEEEEEDDEEEEEEEEE 504
BCL11B		EEEDEEEEEE 543
BOD1L1		DEEEEEEEDE 2997
BRD2		EEEEEEDEEDEEEE 506
BRG1		EEEEEEEE 672
CACNA1D		EEEEEEEDE 836
CACNA1F		EEEEEEEEEEEE 825
CASQ2		EDDDEDDDDD 383
CASZ1		EDDEDEDDDEDDDDEDDDDED 1714
CCDC136		EEEEEEEEE 26
CCDC28B	141	EEEDDEEEED 150
CDK11a		EEEEEEEEEE 304
CDK11a	312	EEEEEEEEEE 324
CDK11b	304	EEEEEEEEEE 316
CDK11b	324	EEEEEEEEEE 336
CELSR2	2743	EEEEEEEEE 2752
CENP-B	406	EEEEEEEEEEE 419

```
CENP-B
            515 EEEDDEEEDDEDEDDDDDEED 535
CERS3
            346 EEEEEEEEE 355
CFAP43
            956 EEDDEEEEED 966
CHD4
            134 EEEEEEDDDDD 144
CHD8
           2537 EEDDDEDEEDDDD 2549
CHIC1
             42 DDDEEDEEEEEEEEEEEEEE 68
            743 DEEEEEDDEDEEE 755
CIZ1
              16 EEEEEEEEDE 25
CLTP3
CLSTN1
             925 EEEEEEEEEE 935
CNGB1
             355 EDEEEEEEEEEEEE 371
            877 EEEEEEEEE 886
CNKSR2
            220 EEEEEEEEE 229
CNPY4
CSPG5
            276 DEEEEEEEDD 285
CSRNP3
            370 DEEEEEEEEEEEEDDDDD 388
Cullin-9
          1671 EEEEEEEEEE 1681
Cullin-9
           2463 EEEEEDDEDD 2472
CWC22
            423 EEDEEEEEEE 432
DAXX
            444 DEEEEEEEEEEE 457
            475 EDDEEEDEEEE 485
DAXX
            1410 EEEDDDEDDDD 1420
DCAF1
           100 EEEEEEEEEEE 112
DCAF8
             126 EEEEEEEEEEEEEEE 147
DCAF8L2
DEK
             33 EEEEDEDDEEEEEEE 47
Dematin
             216 EEEEEEEDDD 225
Dp-2
             432 DEDEEDDEED 441
            300 EEEEEEEEEEEEEEEEEEE 326
EHMT2
            530 DEDEEEEEEEEEEE 547
eIF3D
eIF5B
            532 EEEEEEEEEEEE 546
EP400
            426 EEEEEEEEEEE 437
Ephexin-1 216 EEEEEEEEE 226
ERCC6
            378 EEEEEEEDDE 387
ERCC6-PGBD3 378 EEEEEEEDDE 387
            273 EDDEEEDEDEEEDEDED 289
ESF1
FAM171A1
            858 EEEEDDDDDD 867
FAM193A
             905 EEEEDEEEEED 915
FAM43B
             265 EEDEEEEEDD 274
FAM9A
             262 EEEEEEEEEEE 275
FBX03
             424 EEEEEEEEEDEDDD 438
FGD1
             340 EEEDDEEEEEE 350
             36 EEEEEEEEEE 46
FKBP8
             26 EDEEDEEEEDDDE 38
FOXD1
FOXO3
             59 EEEDDEDDED 68
FOXO3B
            144 EEEDDEDDED 153
            704 EEEEDEEEEEEE 715
GOLGA2
GRWD1
            123 DEEEEEEDEEDEEE 136
GSE1
           1102 EEEEEEDDED 1111
            298 EEEEEEEEDEE 309
GZF1
            260 DEEDEDEEEEEE 272
HAP1
HAX1
             30 DEDDDEEEEEE 40
HDGF
             213 EEEEEEDEEEE 223
HINFP
             49 EEEEEEEEDD 58
            1860 DEDEDEDEEE 1869
HIVEP3
HMGB1
             186 EEEEDEEDEEDEEEEEDEEDEEDEDDDE 215
            186 EEEEDEEDEEDEEDEEDEEDDDDE 211
HMGB1P1
            188 EDEEEEEEEEDEDEEEEDEDEE 209
HMGB2
            181 EEEDEEEEEEEEEEEE 200
HMGB3
hnRNP II
             83 DEEEEEEEEE 94
             74 DEEEDEEEEEEDEE 87
hnRNP UL2
            514 DEEEEEEEE 523
Homez
             526 EDDEEEEEEEEDDDDDDDD 545
Hox-A7
             217 DEEDDDEEEEDEEE 230
HRC
             193 EEEEEEEEEE 204
HRC
             244 EEDDDDDDDDDDDDDDD 261
```

```
541 EEEEEEEDEE 550
          2433 DEEEEEEEDEEDD 2445
HUWE1
IFNLR1
            324 EDEEEEDEED 333
           1014 EEEEEEDDDDDDD 1026
IGSF3
            164 EEEEEEEEEEE 176
IL27
Importin-4 814 DEEEEEEDDD 823
Integrin\alphaE 189 EEEEDEEEEE 198
          211 EEEDEEEDEED 221
IRX3
Kanadaptin 648 EEEEEEEEE 658
KANK1 1033 EEEEEEEDED 1042
          1070 EEEEEEEEEEEEEEEEEEEE 1104
KAT6B
          1351 EEEEEEEEEEEEEEE 1368
KAT6B
            123 EEEEDEEEEEEEEE 137
KCNA4
             67 DDDEDDEEDE 76
KCNN1
            856 EEEEEEEEEEDD 868
KDM2A
KIF21A
            611 EDEEEEEEEEDD 623
            250 EEEEEEEEDEEE 261
KRT1
LAS1L
            589 EEEEEDEDDEDDEEED 604
LDOC1
            132 DDDEDDDDEEEEDD 145
Leiomodin-3 144 DEEDEEEEDDDDDDE 158
LMTK3 1279 EDEDEDEEEDEE 1290
           107 EDDEEDDDEE 116
MAPK8IP1
MAPK8IP2
             88 EEEDDEDEEEEEEEE 103
            469 EEEDEEDDEEEED 481
MAPK8IP2
MBD3
            268 EDDDEEDEEEEEE 281
Midasin
            4781 DDDEEEDEEED 4792
MIER1
             83 EEDEEEEEEEE 94
            357 EEDEDEDDED 366
MNX1
            340 DEDEDDDDEED 350
mTERF4
            372 DEDEDDDEEE 381
mTERF4
mTERF4
            357 DEDDDDEDDDE 367
          357 DEDDDDEDDDE 367
1002 EEEEEEEEEE 1012
MYO15B
MYT1
            258 EEEDEEEEEEEEEEEEEEEEEEEEEEEEEEEEEE 306
MYT1L
            136 EEEDEDDDED 145
MYT1L
            150 EDEEEEEEEEEEEE 167
            264 DDEDDEEEDEEEE 276
N-Myc
N-WASP
            486 DEDEDEDDEED 496
           213 EEEEEEEEDD 223
NAP1L2
Nardilysin 150 EEEEEDDDED 159
NBPF4
             167 DEDEDEDEDD 176
             167 DEDEDEDEDD 176
NBPF5P
NBPF6
             167 DEDEDEDEDD 176
             703 EEEEDEEDEEEEDE 716
NBR1
            344 EEEEEEEEEEEEED 360
NCBP3
Neurabin-2 411 EEDDEDDEED 420
            67 EEEEEEEEEDDD 78
82 EEEEEEEEEE 91
NEUROD1
NEUROD2
Nischarin 637 EEEDEEEEEED 648
           672 EEEEEEEEDEE 682
Nischarin
NPM1
            161 DEDDDDDDEEDDDEDDDDD 180
NPM2
            137 EEEEEEEEDDEDED 150
NT5C2
           549 DEDDDEEEEEEE 561
Nucleolin 154 EEDEEDDEDEDEDE 169
Nucleolin 185 EDEDDEDDEDDEDDDDDEED
            185 EDEDDEDDEDDEDDDDEEDD 205
            234 EDEDEEEDDEDEDDDDDEDDEDDEDDEEEEEEEEE 271
Nucleolin
OS-9
             414 EEEEDEDEDEDEDE 429
PAK3
             187 EEEDEEEEEEDE 199
PATL2
             35 EEEEEEEDEED 45
            189 EEEEEEEEEE 200
PAXIP1
             91 EEEEEEEED 100
PCGF6
            666 EEEDEEEEEE 675
PDE4C
PDIA4
             39 EDEEEEEEEDDDEEEDD 55
PELP1
             87 DEEEEEEEEEEEEEEE 909
```

```
943 EEEEEEEDEEEEE 956
PERCC1
             34 EEEEEEEEEEEE 47
Peregrin
             465 EEDEDEEEDE 474
            324 EDEEDEEDDD 333
PEX14
PHACTR1
            395 EEEEEEEDEDDD 406
PHACTR2
             453 DDEDEDEDED 462
             248 EEEEEEEEEEE 261
PHF23
PIAS4
             477 EDEEEEEEEEEDEDEE 492
PIK3R5
             319 DDEEEEEEEE 329
PLC \beta3
             556 EDEEEDEEEEE 566
PLC \delta3
            499 EEEEEDDEEEEEE 511
            712 EEEEEEEEEEE 723
PLEKHG5
PLPPR3
             441 EEEEEEEDEEEEEEEEEE 461
             600 EEEEEEEEEE 611
Podocan
PODXL2
             162 EEEEEEEEEE 172
             430 EEEDEEEEEEEEE 444
PPARGC1B
PPARGC1B
             814 EEEEEDDEEED 824
PPM1F
             101 EEEEEEEDDDEEE 113
PPM1G
             302 EEDDEEEEEE 311
             351 EEEEDEEEDED 361
PPP1R15A
PPP1R1B
            119 EEDEEEEEDDEEEEEED 136
            298 EEDEEEDEEEEE 310
PPP4R2
           808 DDDEDDDEDED 818
PPP4R3A
PPP4R3B
            829 DDEEEDEEEE 838
            621 DDDEEEEDEEE 631
PPP6R1
PPP6R1
            671 EDEEEEDEEEEDEE 685
            134 EEEDEDEDED 143
PRDM10
            268 EEEEEEEEEDEEEEEDDDDDE 288
PRDM2
            313 EEEEEEEEEEE 325
PRKCSH
PTMS
             63 EEEDEEEEEEDDE 75
RAD21
             534 EDDEEEEDED 543
RanGAP1
             359 DDEDEEEEEE 368
            377 EEEEEEDEEEEEEEEEEE 397
RanGAP1
RBM10
             113 EEEEEEEDEEEEE 125
RBM19
            714 EEEEEEEEEE 725
            234 DDDDDDDDDEED 244
RBM28
Reticulon-4
             32 EDEEEEEEEEEDEDED 48
            222 EDDDDDDDDDDDDEEE 237
            195 EDDEDEDEDED 205
RNGTT
RRP12
           1054 EEEEEEEEEE 1064
RSPH4A
            567 EEEEEEEDEE 576
RYR1
           1873 EEEEEEDEEEE 1883
            764 EEEEEEDEEEEED 776
SALL2
SCAF1
             268 EEEEEEEEEEEEEEE 288
SCAF1
           1022 EEEEEEEEEEEEEE 1039
             377 DDEEEEEEDEE 387
Sec24B
SEC63
             750 EEEEEEEDDD 760
            989 EEEEDEDEEEEED 1001
SECISBP2L
             76 EEEEEEEEEEDEDEEEE 92
SENP3
            246 EEDDDDDDEEEE 256
SET
            977 DEEDDEEDEEDED 989
SETD1A
SETD1B
           1185 EEEEEEEEE 1194
Shroom4
           1132 EEEEEEEEEEEEEEEE 1151
            419 EEEEEEEEE 428
SKIDA1
SLC24A1
            879 EEEEEEEEEE 890
SLC24A3
            421 DEEEEEDEDDDE 432
            135 DEEEEEEEEE 145
SLC4A3
SMARCA2
           1518 EEEEEEDEEE 1527
SMYD5
            393 EEEEEEEEEE 403
SNAPC5
             86 EEEEEEEEE 95
             383 DDEDEEEEEE 392
SNIP1
SNRK
             446 EEDEEEDEED 455
SNX21
             67 EDDEDDEDEDDEE 79
```

```
SOX-11
             223 DEDDDDDDDDDD 234
SOX-12
             163 EDDDEDDDEE 172
SPRYD3
             373 EEEEEEEEEED 384
              43 EDEEEEEEEE 53
SPT5
SPT5
              55 DEEEEEEDDD 64
              32 EEEDDDEEEEEE 43
SPT6
              65 EEEEEEEEEE 76
STAC3
            1827 EEEEDEEEEE 1836
TAF1
TAF7L
             333 DDDEDEDDEDEDEDEDEDED 354
TAF9
             249 EDDDDDDDDDDD 260
TAOK2
             378 EEEEEEEEEEEE 392
             607 EEEEEEEEEEEE 621
Taperin
TF3C-γ
             94 EDDEEEEEEEEEEE 111
             486 EDEEDEEEEEEED 500
TF3C-ε
TIMELESS
             666 EEEEEEEEEEE 678
             240 DDEDEEEEEEE 251
TMED8
TPR
            1966 EEDEEDDDDDEDD 1978
TRANK1
            1087 EEEEEEEDEEEED 1099
             421 DEEEEEEEEEE 432
TRIM26
            122 DEEEEEEEED 131
TRIM52
           1262 EEEEEEEEEEE 1274
TSPOAP1
           1334 EEEEEEEEDEEEE 1346
TSPOAP1
            733 EEEEEEEEDEEEEEDEEEEEEEEEEEEEEE 771
TTLL3
             71 EDEDEDEDEE 80
            115 EDEEEEEEEDEEDEEEE 131
TULP1
TUT7
            845 DEEEEDDEEEEEEE 859
UBTF
            678 EEDDEEDEDDEDEDEEEEDDE 698
            725 EEDDEDEDDDEDDDEDED 742
UBTF
URI1
             299 DDDDDDDDDDDDD 311
             84 EEEEEDEEEEEED 97
UTP25
VGLL3
              64 EEEDEEEEEEE 74
VIRMA
             258 EEEEDEDEDD 267
             276 EEEEEDEEEE 285
VIRMA
VSIG10
             463 EEEEEEEEEED 475
            154 EEEEEEEEEE 164
WDR70
             34 EEEEEEEEE 43
WEE1
Wiz
            567 EEEEEEEEED 577
YTHDC1
            230 EEEEEEEEEEEEEE 249
             43 EEEEEDDDDED
ZBTB12
            195 EEEDEDEDED 204
ZBTB4
             637 EEDEEEEDEEEEEDEEE 654
ZBTB47
             277 DEEEEDDEEEEEEEEE 294
             326 EEEEEEEEE 335
ZBTB47
            140 EDDDDDEDDDDEEDEEEEEEEEDDDDD 167
ZBTB7C
ZBTB9
             212 EEEEEEEEDDDDED 225
            1062 DEEEEEEEE 1071
ZEB1
ZFHX3
             473 EEEEEEEEEEEEE 489
ZFTA
             188 EEEEEEEEEEE 200
            116 EEEEEEDEEEE 126
ZMYND15
            135 EEEEEEEEDEDEDD 148
ZNF316
            498 EEEEDEDEEEE 508
ZNF326
ZNF428
             43 EEEEDEEEEEE 54
ZNF526
             232 EEEEEDDEEDEEDDEE 247
             457 DEEEEEEEEDE 467
ZNF777
ZNF830
            160 EDEEEEEEEE 170
```

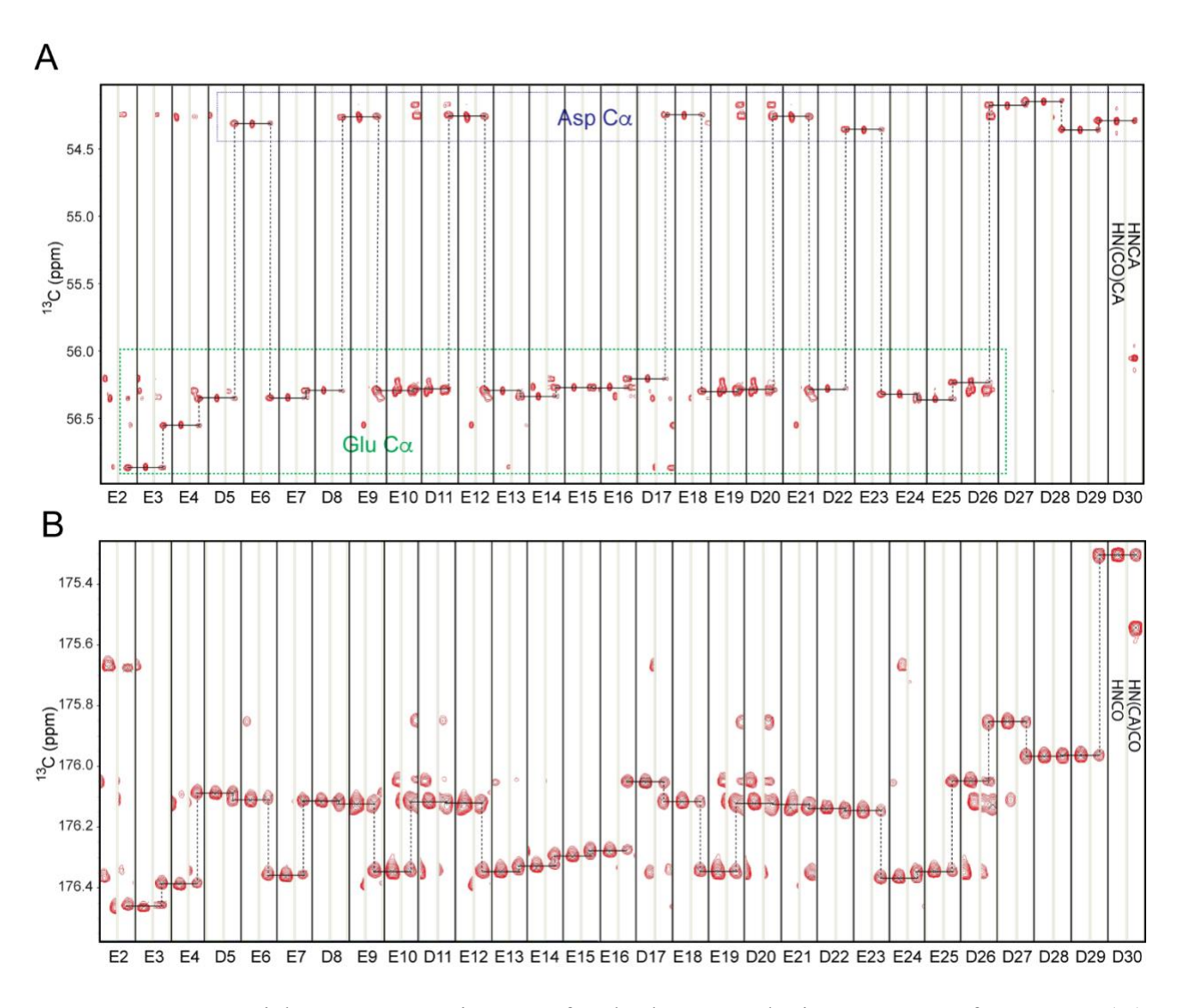


Figure S1. Sequential resonance assignment for the low-complexity sequence of DERT30. (**A**) 13 C $_{\alpha}$ connectivity through the HNCA and HN(CO)CA spectra. (**B**) Backbone 13 C=O connectivity through the HN(CA)CO and HNCO spectra.

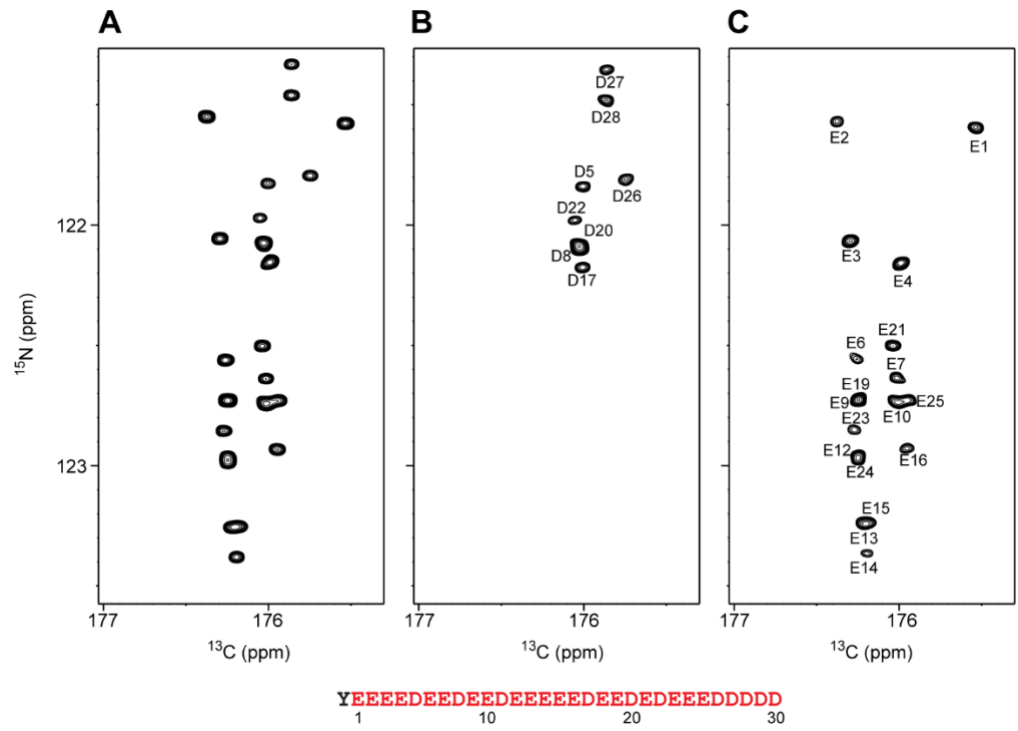


Figure S2. Direct ¹³C-detected CON spectra recorded with and without an amino-acid type-selective filter⁵ for ¹³C, ¹⁵N-labeled DERT30. (**A**) CON spectrum recorded without any amino-acid type-selective filter. (**B**) Asp/Asn-selective CON spectrum. (**C**) Gln/Glu-selective CON spectrum. The annotations in Panels B and C indicate ¹³C=O assignment. Note that the annotations in Figure 1B indicate ¹⁵N resonance assignment.

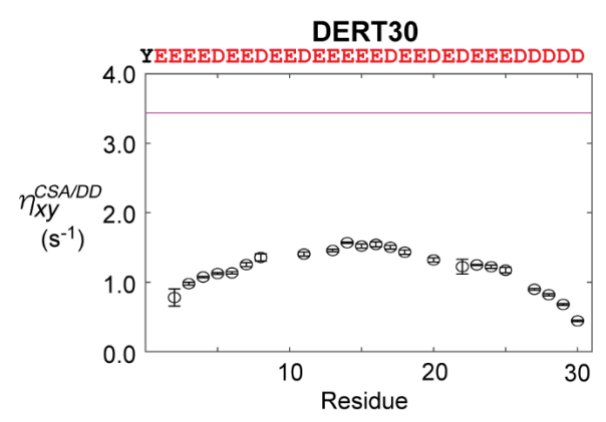


Figure S3. Transverse ¹⁵N CSA / ¹⁵N-¹H DD cross-correlation rates⁴⁰⁻⁴² measured for DERT30 NH groups. The purple line indicates the theoretical values for a rigid system with a rotational correlation time of 2 ns and an NH order parameter of 0.9. The observed values of the cross-correlation rates suggest the disordered nature of DERT30.

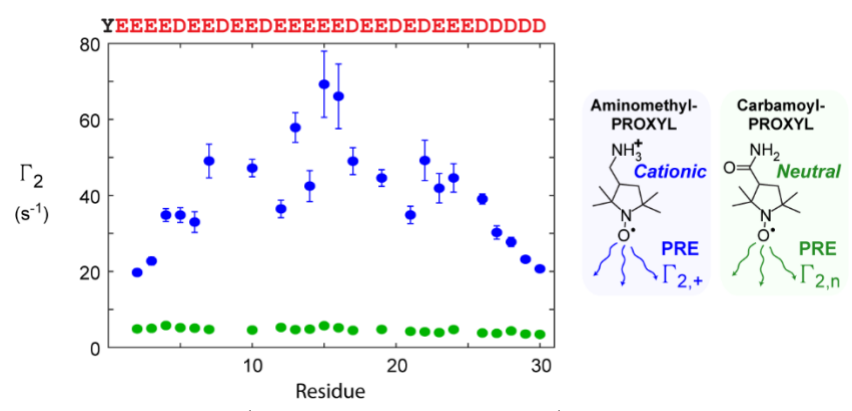


Figure S4. Solvent PRE data for ${}^{1}H_{\alpha}$ nuclei of DERT30. ${}^{1}H$ transverse PRE rates (Γ_{2}) measured for individual residues of DERT30 at 25°C and the ${}^{1}H$ frequency of 800 MHz in the presence of 20 mM aminomethyl-PROXYL or 20 mM carbamoyl-PROXYL. The solvent PRE data for aminomethyl-PROXYL and carbamoyl-PROXYL are shown in blue and green, respectively.

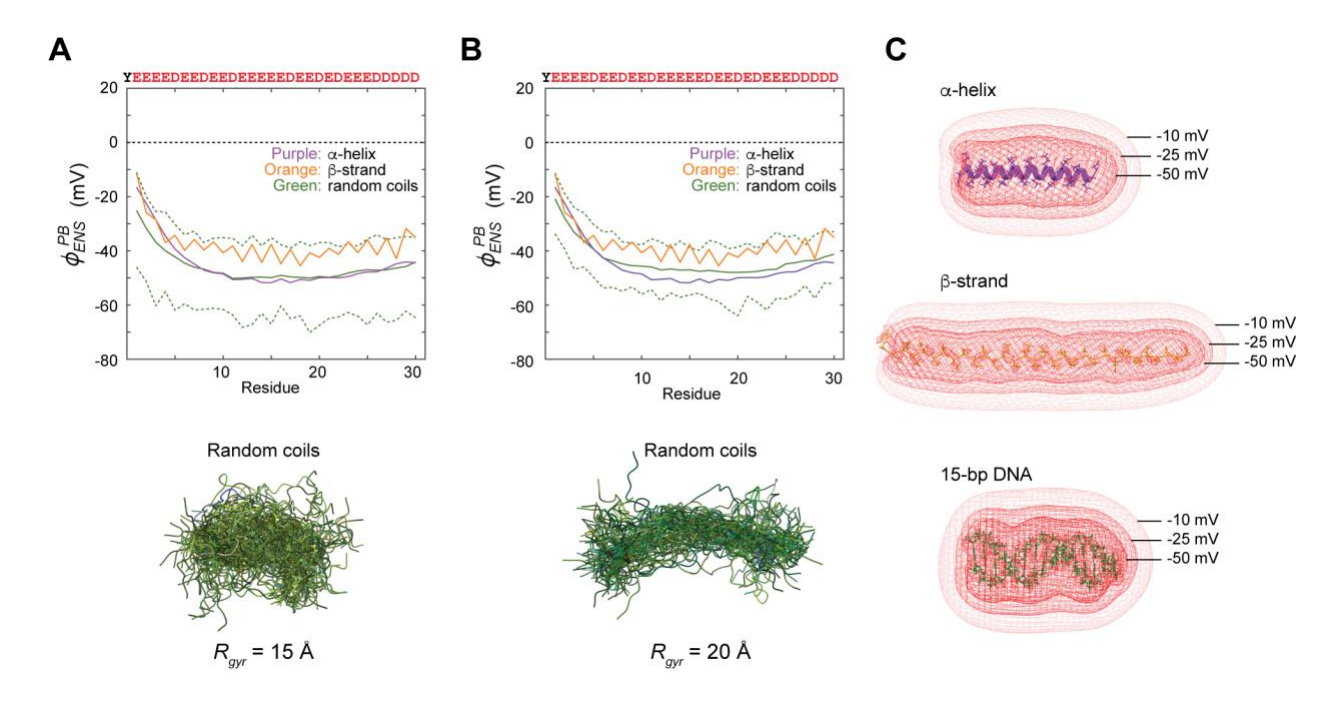


Figure S5. Poisson-Boltzmann equation-based prediction of ϕ_{ENS} potentials for structural models of DERT30. Predictions for an α-helix (purple) and an extended β-strand (orange), and 100 random coils (green) are shown. For the random coils, the average values are indicated in the green solid line and the minimum and maximum values are indicated in the green dotted lines. Structural models used to predict the ϕ_{ENS} potentials around DERT30. (**A, B**) Results for the random-coil structure ensembles with a radius of gyration $R_{gyr} = 15$ Å (Panel A) or 20 Å (Panel B). The mean O-O distance between the closest carboxylate groups was 4.6 and 4.7 Å for the ensembles in Panel A and B, respectively. These O-O distances are shorter than the corresponding distance (5.7 Å) between closest phosphate groups (O_{1P} or O_{2P} atoms) in B-form DNA. (**C**) Isopotential maps of electrostatic potentials at -50, -25, and -10 mV computed for DERT30 adopting an α-helix or β-strand structure and for 15-bp DNA. The electrostatic potentials were calculated using APBS²⁰, and the isopotential contours were drawn with ChimeraX⁴³.

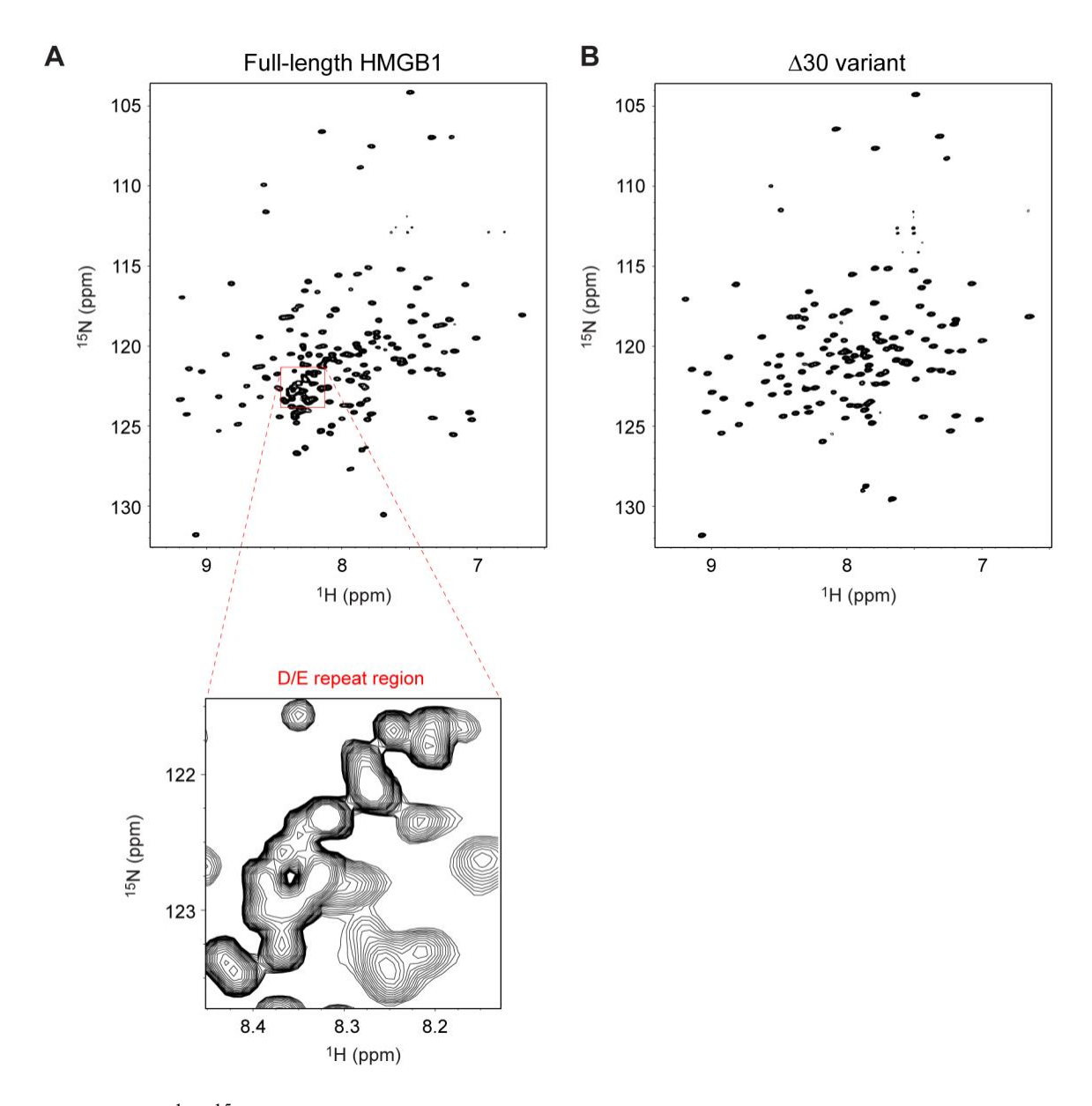


Figure S6. $^{1}\text{H-}^{15}\text{N}$ TROSY spectra recorded at 25°C for the full-length HMGB1 protein and the $\Delta30$ variant dissolved in a buffer of 10 mM potassium phosphate, 100 mM NaCl, and 5% D₂O at pH 7.4. These proteins are in the oxidized form with the C23-C45 disulfide bond. 3,44

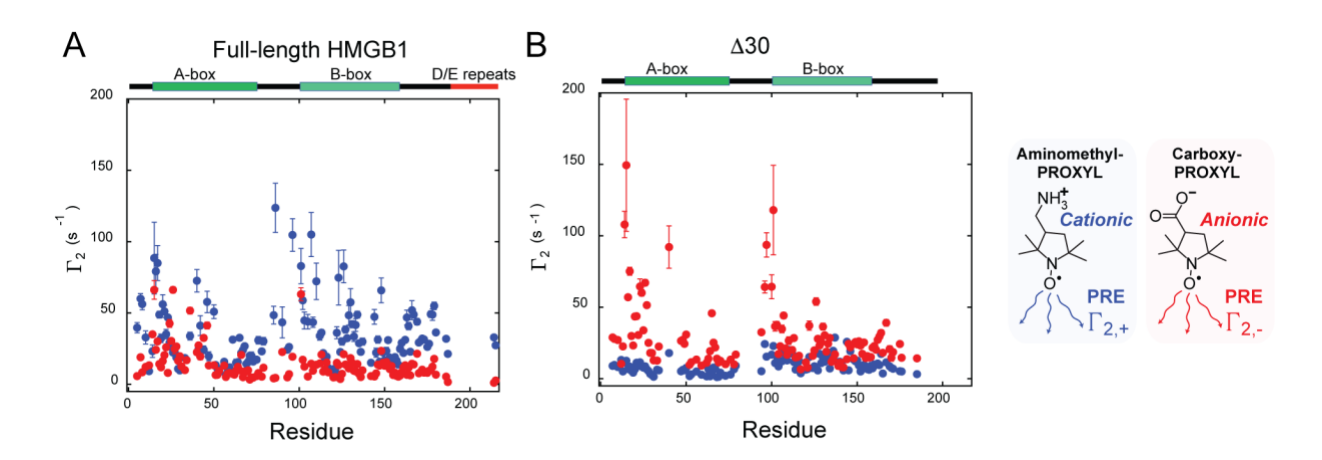


Figure S7. Solvent PRE rates Γ_2 measured for backbone 1H_N nuclei of the full-length HMGB1 protein (Panel A) and the $\Delta 30$ variant lacking the D/E repeats (Panel B). The paramagnetic cosolute was either 20 mM aminomethyl-PROXYL (blue) or 20 mM carboxy-PROXYL (red).

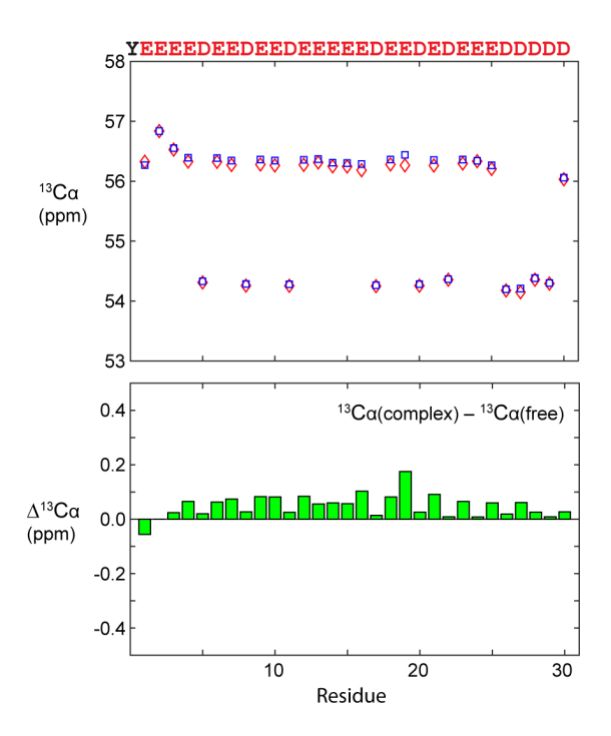


Figure S8. 13 C $_{\alpha}$ chemical shifts of DERT30 in the free state (red diamonds) and in the complex with the $\Delta 30$ variant of HMGB1 (blue squares). The 13 C $_{\alpha}$ chemical shifts were referenced to internal DSS. The differences between the two states are indicated by green bars. Note that the changes in 13 C $_{\alpha}$ chemical shifts are small while changes in 14 N and 15 N chemical shifts are large as shown in Figure 4A. These data show that DERT30 lacks secondary structures even when DERT30 is bound to $\Delta 30$.

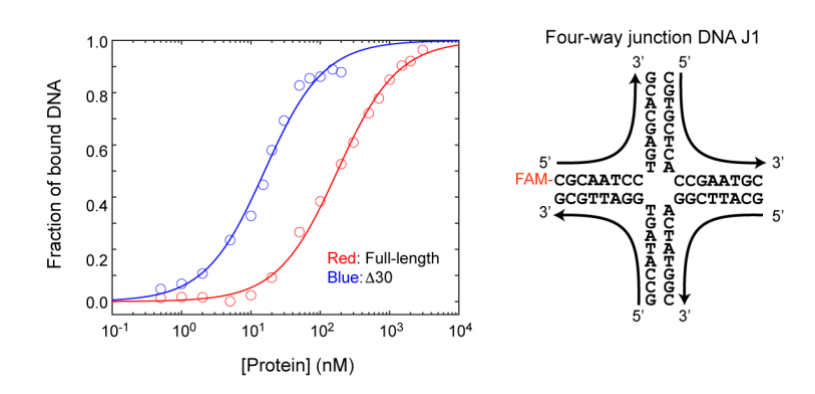


Figure S9. Fluorescence anisotropy-based binding assay data used to determine the dissociation constants K_d of the full-length HMGB1 and $\Delta 30$ variant proteins for the FAM-labeled four-way junction DNA J1. The buffer conditions were 10mM potassium phosphate (pH 7.4) and 150 mM NaCl. The dissociation constants K_d for the full-length HMGB1 and $\Delta 30$ variant proteins were 180 \pm 10 nM and 15 \pm 2 nM, respectively.

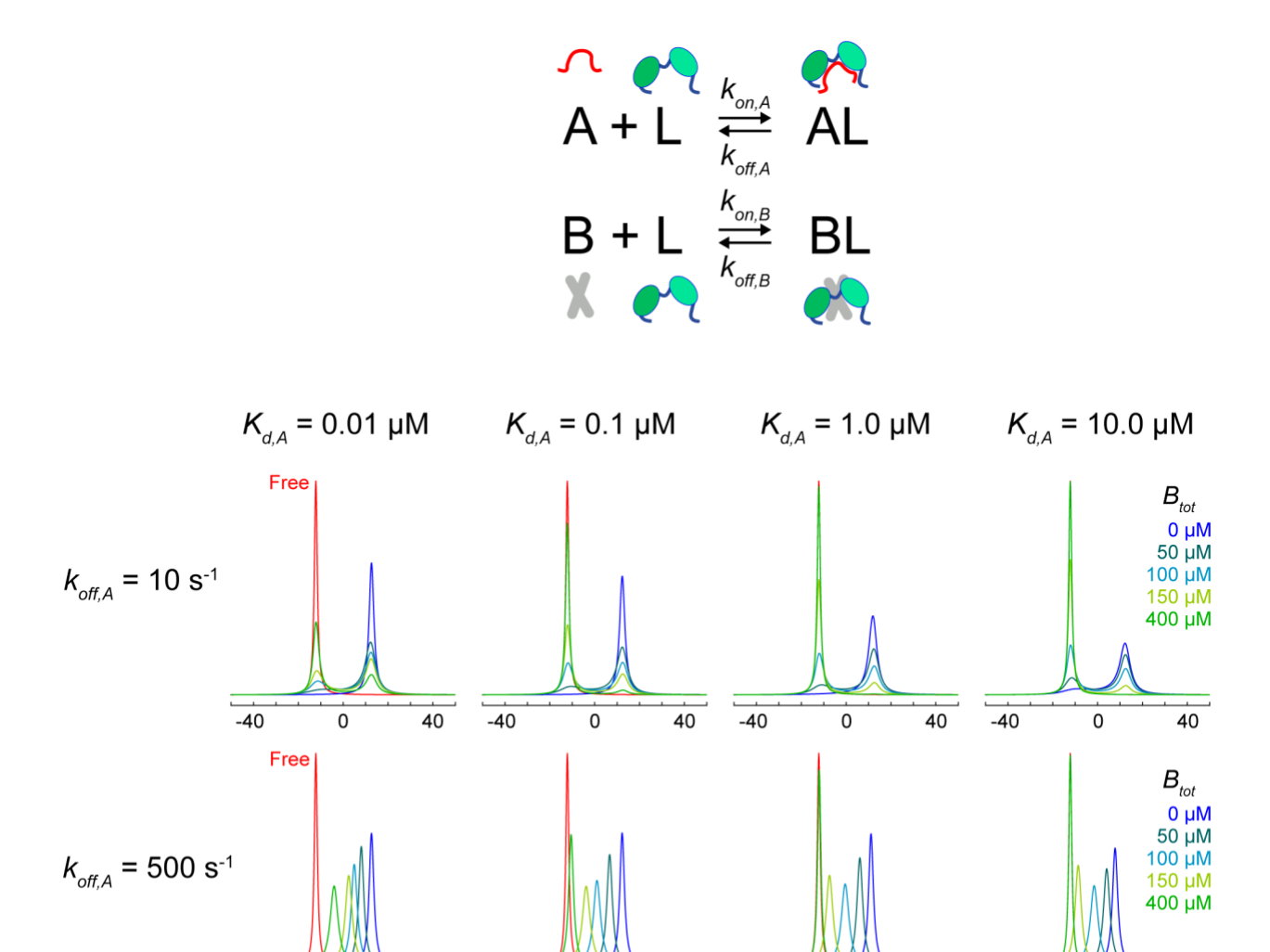


Figure S10. Bloch-McConnell equation-based simulations of the NMR-based competition data shown in Figure 4A. In the scheme shown above, the molecules A, B, and L correspond to 15 N-labeled DERT30, unlabeled DNA J1, and unlabeled Δ30 protein. 15 N NMR line shapes for 15 N DERT30 were simulated using Eqs. s9-s18 together with $A_{tot} = [A]+[AL] = 200 \,\mu\text{M}$, $L_{tot} = [L] + [AL] + [BL] = 200 \,\mu\text{M}$, $|\Omega_A - \Omega_{AL}|/(2\pi) = 25 \,\text{Hz}$ (based on the data shown in Figure 4A), $R_{2,A} = 5 \,\text{s}^{-1}$, $R_{2,AL} = 8 \,\text{s}^{-1}$, $K_{d,B} = 0.015 \,\mu\text{M}$ (based on the results shown in Figure S9), and the indicated parameters. The simulations were performed using MATLAB scripts similar to those given in the Supporting Information of Sahu and Iwahara. 45 It should be noted that when the exchange between A and AL is in a fast exchange regime (e.g., with $k_{off,A} = 500 \,\text{s}^{-1}$), the apparent chemical shift of A (15 N DERT30) depends on the total concentration of the competitor molecule B (DNA J1) regardless of the timescale of the exchange between B and BL.

-40

40

-40

0

40

Frequency (Hz)

-40

0

40

-40

0

40

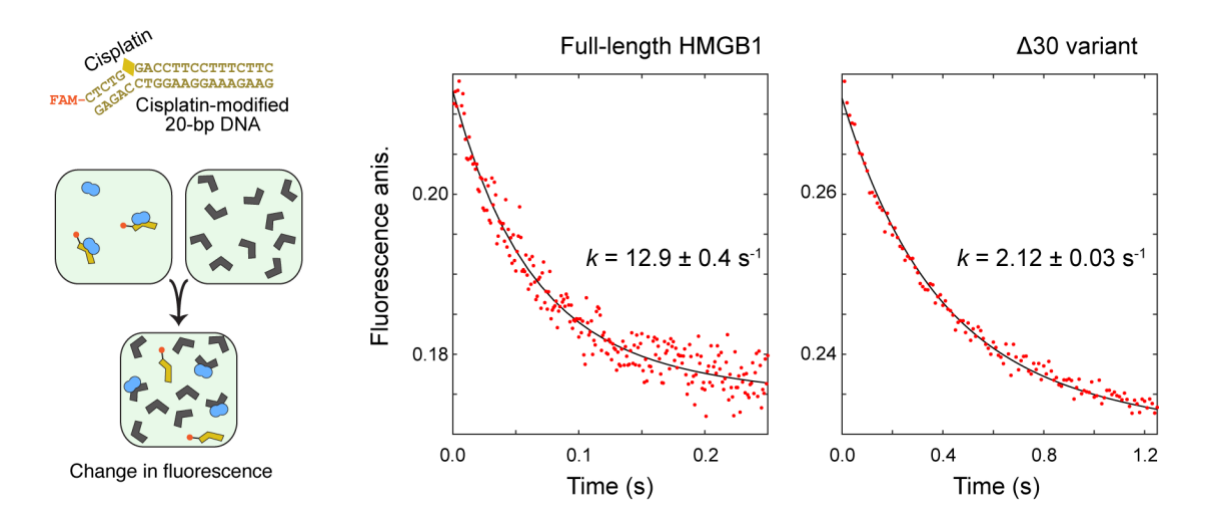


Figure S11. Stopped-flow fluorescence time-course data on the kinetics of protein dissociation from cisplatin-modified 20-bp DNA (cisGG20). To measure the rate constants reported in Figure 4B, a solution of a complex formed with 50 nM protein (either full-length HMGB1 or $\Delta 30$) and 10 nM FAM-labeled cisGG20 was mixed with a solution of unlabeled cisGG20. Shown here are fluorescence time-course data from the stopped-flow experiments with 1.75 μM unlabeled cisGG20. Because the dissociation kinetics of the full-length HMGB1 protein was remarkably faster, different time intervals were used for the two proteins. The time intervals were 1 ms for the full-length HMGB1 protein and 10 ms for the $\Delta 30$ variant. Note that the time range is different for the two graphs.

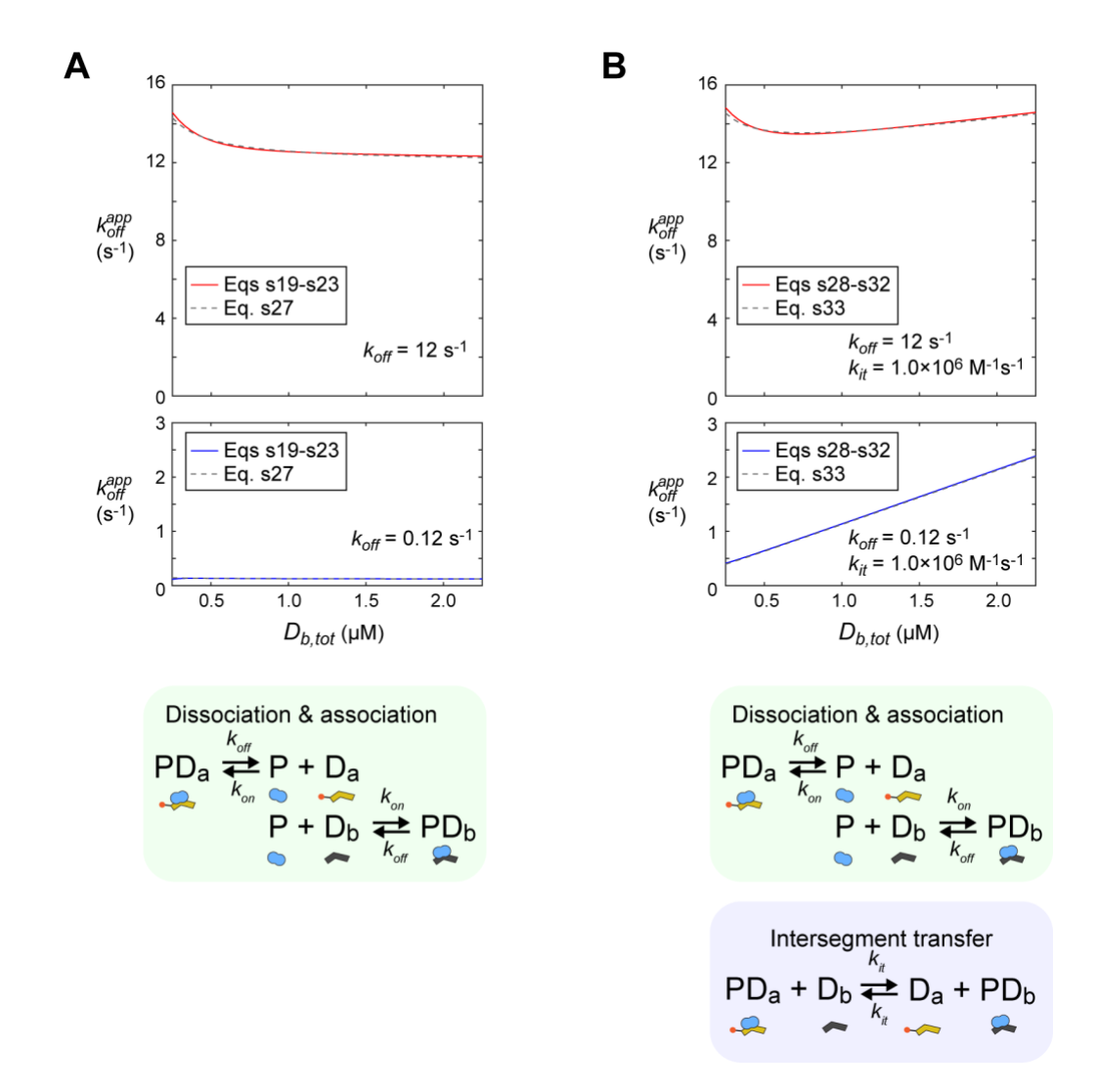


Figure S12. Simulations of the apparent dissociate rate constants in the stopped-flow experiment. Panel A shows the simulations for systems involving dissociation and association, whereas Panel B shows the simulations for systems involving intersegment transfer in addition to dissociation and association. The red and blue curves were obtained using the time course obtained with the rate equations (Eqs. s19-s23 for A and Eqs. s28-s32 for B). The rate equations were numerically solved using an ordinary-differential-equations solver ('ode23s') of the MATLAB software. The gray dotted lines were obtained with the approximate analytical expression (Eq. s27 for A and Eq. s33 for B). $P_{tot} = 50$ nM, $D_{a,tot} = 10$ nM, and $k_{on} = 1.2 \times 10^9$ M⁻¹ s⁻¹ were used along with the values of k_{off} , k_{it} , and $D_{b,tot}$ indicated in the graphs.

References for Supporting Information

- 1. Wang, X.; Greenblatt, H. M.; Bigman, L. S.; Yu, B.; Pletka, C. C.; Levy, Y.; Iwahara, J., Dynamic Autoinhibition of the Hmgb1 Protein Via Electrostatic Fuzzy Interactions of Intrinsically Disordered Regions. *J Mol Biol* **2021**, *433*, 167122.
- 2. Kallenbach, N. R.; Ma, R.-I.; Seeman, N. C., An Immobile Nucleic Acid Junction Constructed from Oligonucleotides. *Nature* **1983**, *305*, 829-831.
- 3. Wang, X.; Mayorga-Flores, M.; Bien, K. G.; Bailey, A. O.; Iwahara, J., DNA-Mediated Proteolysis by Neutrophil Elastase Enhances Binding Activities of the Hmgb1 Protein. *J Biol Chem* **2022**, *298*, 102577.
- 4. Cavanagh, J.; Fairbrother, W. J.; Palmer, A. G., III; Rance, M.; Skelton, N. J., *Protein Nmr Sprectroscopy: Principles and Practice*. 2 ed.; Elsevier Academic Press: Burlignton, 2007.
- 5. Bermel, W.; Bertini, I.; Chill, J.; Felli, I. C.; Haba, N.; Kumar M. V, V.; Pierattelli, R., Exclusively Heteronuclear 13c-Detected Amino-Acid-Selective Nmr Experiments for the Study of Intrinsically Disordered Proteins (Idps). *ChemBioChem* **2012**, *13*, 2425-2432.
- 6. Felli, I. C.; Pierattelli, R., ¹³c Direct Detected Nmr for Challenging Systems. *Chem Rev* **2022**, *122*, 9468-9496.
- 7. Delaglio, F.; Grzesiek, S.; Vuister, G. W.; Zhu, G.; Pfeifer, J.; Bax, A., Nmrpipe a Multidimensional Spectral Processing System Based on Unix Pipes. *J Biomol NMR* **1995**, *6*, 277-293.
- 8. Lee, W.; Tonelli, M.; Markley, J. L., Nmrfam-Sparky: Enhanced Software for Biomolecular Nmr Spectroscopy. *Bioinformatics* **2015**, *31*, 1325-1327.
- 9. Yu, B.; Pletka, C. C.; Pettitt, B. M.; Iwahara, J., De Novo Determination of near-Surface Electrostatic Potentials by Nmr. *Proc Natl Acad Sci U S A* **2021**, *118*, e2104020118.
- 10. Yu, B.; Pletka, C. C.; Iwahara, J., Protein Electrostatics Investigated through Paramagnetic Nmr for Nonpolar Groups. *J Phys Chem B* **2022**, *126*, 2196-2202.
- 11. Yu, B.; Wang, X.; Iwahara, J., Measuring Local Electrostatic Potentials around Nucleic Acids by Paramagnetic Nmr Spectroscopy. *J Phys Chem Lett* **2022**, *13*, 10025-10029.
- 12. Schwieters, C. D.; Bermejo, G. A.; Clore, G. M., Xplor-Nih for Molecular Structure Determination from Nmr and Other Data Sources. *Protein Sci* **2018**, *27*, 26-40.
- 13. Lipsitz, R. S.; Sharma, Y.; Brooks, B. R.; Tjandra, N., Hydrogen Bonding in High-Resolution Protein Structures: A New Method to Assess Nmr Protein Geometry. *J Am Chem Soc* **2002**, *124*, 10621-10626.

- 14. Grishaev, A.; Bax, A., An Empirical Backbone-Backbone Hydrogen-Bonding Potential in Proteins and Its Applications to Nmr Structure Refinement and Validation. *J Am Chem Soc* **2004**, *126*, 7281-7292.
- 15. Bermejo, G. A.; Clore, G. M.; Schwieters, C. D., Smooth Statistical Torsion Angle Potential Derived from a Large Conformational Database Via Adaptive Kernel Density Estimation Improves the Quality of Nmr Protein Structures. *Protein Sci* **2012**, *21*, 1824-1836.
- 16. Kuszewski, J.; Gronenborn, A. M.; Clore, G. M., Improving the Packing and Accuracy of Nmr Structures with a Pseudopotential for the Radius of Gyration. *J Am Chem Soc* **1999**, *121*, 2337-2338.
- 17. Kohn, J. E.; Millett, I. S.; Jacob, J.; Zagrovic, B.; Dillon, T. M.; Cingel, N.; Dothager, R. S.; Seifert, S.; Thiyagarajan, P.; Sosnick, T. R., et al., Random-Coil Behavior and the Dimensions of Chemically Unfolded Proteins. *Proc Natl Acad Sci U S A* **2004**, *101*, 12491-12496.
- 18. Dolinsky, T. J.; Nielsen, J. E.; McCammon, J. A.; Baker, N. A., Pdb2pqr: An Automated Pipeline for the Setup of Poisson-Boltzmann Electrostatics Calculations. *Nucleic Acids Res* **2004**, *32*, W665-667.
- 19. Dolinsky, T. J.; Czodrowski, P.; Li, H.; Nielsen, J. E.; Jensen, J. H.; Klebe, G.; Baker, N. A., Pdb2pqr: Expanding and Upgrading Automated Preparation of Biomolecular Structures for Molecular Simulations. *Nucleic Acids Res* **2007**, *35*, W522-525.
- 20. Jurrus, E.; Engel, D.; Star, K.; Monson, K.; Brandi, J.; Felberg, L. E.; Brookes, D. H.; Wilson, L.; Chen, J.; Liles, K., et al., Improvements to the Apbs Biomolecular Solvation Software Suite. *Protein Sci* **2018**, *27*, 112-128.
- 21. Greenfeld, M.; Herschlag, D., Probing Nucleic Acid—Ion Interactions with Buffer Exchange-Atomic Emission Spectroscopy. In *Biophysical, Chemical, and Functional Probes of Rna Structure, Interactions and Folding: Part B*, 2009; pp 375-389.
- 22. Bai, Y.; Greenfeld, M.; Travers, K. J.; Chu, V. B.; Lipfert, J.; Doniach, S.; Herschlag, D., Quantitative and Comprehensive Decomposition of the Ion Atmosphere around Nucleic Acids. *J Am Chem Soc* **2007**, *129*, 14981-14988.
- 23. Das, R.; Travers, K. J.; Bai, Y.; Herschlag, D., Determining the Mg2+ Stoichiometry for Folding an Rna Metal Ion Core. *J Am Chem Soc* **2005**, *127*, 8272-8273.
- 24. Gebala, M.; Herschlag, D., Quantitative Studies of an Rna Duplex Electrostatics by Ion Counting. *Biophys J* **2019**, *117*, 1116-1124.
- 25. Gebala, M.; Bonilla, S.; Bisaria, N.; Herschlag, D., Does Cation Size Affect Occupancy and Electrostatic Screening of the Nucleic Acid Ion Atmosphere? *J Am Chem Soc* **2016**, *138*, 10925-10934.

- 26. Gebala, M.; Giambasu, G. M.; Lipfert, J.; Bisaria, N.; Bonilla, S.; Li, G.; York, D. M.; Herschlag, D., Cation-Anion Interactions within the Nucleic Acid Ion Atmosphere Revealed by Ion Counting. *J Am Chem Soc* **2015**, *137*, 14705-14715.
- 27. Pletka, C. C.; Nepravishta, R.; Iwahara, J., Detecting Counterion Dynamics in DNA-Protein Association. *Angew Chem Int Ed Engl* **2020**, *59*, 1465-1468.
- 28. Yu, B.; Bien, K. G.; Pletka, C. C.; Iwahara, J., Dynamics of Cations around DNA and Protein as Revealed by ²³na Diffusion Nmr Spectroscopy. *Anal Chem* **2022**, *94*, 2444-2452.
- 29. Yu, B.; Bien, K. G.; Wang, T.; Iwahara, J., Diffusion Nmr-Based Comparison of Electrostatic Influences of DNA on Various Monovalent Cations. *Biophys J* **2022**, *121*.
- 30. Yu, B.; Pletka, C. C.; Iwahara, J., Quantifying and Visualizing Weak Interactions between Anions and Proteins. *Proc Natl Acad Sci U S A* **2021**, *118*, e2015879118.
- 31. Hayamizu, K.; Price, W. S., A New Type of Sample Tube for Reducing Convection Effects in Pgse-Nmr Measurements of Self-Diffusion Coefficients of Liquid Samples. *J Magn Reson* **2004**, *167*, 328-333.
- 32. Wu, D. H.; Chen, A. D.; Johnson, C. S., An Improved Diffusion-Ordered Spectroscopy Experiment Incorporating Bipolar-Gradient Pulses. *J Magn Reson*, Ser A **1995**, 115, 260-264.
- 33. Holz, M.; Weingartner, H., Calibration in Accurate Spin-Echo Self-Diffusion Measurements Using ¹h and Less-Common Nuclei. *J Magn Reson* **1991**, *92*, 115-125.
- 34. Johnson, C. S., Diffusion Ordered Nuclear Magnetic Resonance Spectroscopy: Principles and Applications. *Prog NMR Spect* **1999**, *34*, 203-256.
- 35. Zandarashvili, L.; Nguyen, D.; Anderson, K. M.; White, M. A.; Gorenstein, D. G.; Iwahara, J., Entropic Enhancement of Protein-DNA Affinity by Oxygen-to-Sulfur Substitution in DNA Phosphate. *Biophys J* **2015**, *109*, 1026-1037.
- 36. Itoh, Y.; Murata, A.; Takahashi, S.; Kamagata, K., Intrinsically Disordered Domain of Tumor Suppressor P53 Facilitates Target Search by Ultrafast Transfer between Different DNA Strands. *Nucleic Acids Res* **2018**, *46*, 7261-7269.
- 37. Esadze, A.; Iwahara, J., Stopped-Flow Fluorescence Kinetic Study of Protein Sliding and Intersegment Transfer in the Target DNA Search Process. *J Mol Biol* **2014**, *426*, 230-244.
- 38. Doucleff, M.; Clore, G. M., Global Jumping and Domain-Specific Intersegment Transfer between DNA Cognate Sites of the Multidomain Transcription Factor Oct-1. *Proc Natl Acad Sci U S A* **2008,** *105*, 13871-13876.
- 39. Esadze, A.; Kemme, C. A.; Kolomeisky, A. B.; Iwahara, J., Positive and Negative Impacts of Nonspecific Sites During Target Location by a Sequence-Specific DNA-Binding Protein: Origin of the Optimal Search at Physiological Ionic Strength. *Nucleic Acids Res* **2014**, *42*, 7039-7046.

- 40. Kroenke, C. D.; Loria, J. P.; Lee, L. K.; Rance, M.; Palmer, A. G., Longitudinal and Transverse H-1-N-15 Dipolar N-15 Chemical Shift Anisotropy Relaxation Interference: Unambiguous Determination of Rotational Diffusion Tensors and Chemical Exchange Effects in Biological Macromolecules. *J Am Chem Soc* **1998**, *120*, 7905-7915.
- 41. Tjandra, N.; Szabo, A.; Bax, A., Protein Backbone Dynamics and N-15 Chemical Shift Anisotropy from Quantitative Measurement of Relaxation Interference Effects. *J Am Chem Soc* **1996**, *118*, 6986-6991.
- 42. Pelupessy, P.; Espallargas, G. M.; Bodenhausen, G., Symmetrical Reconversion: Measuring Cross-Correlation Rates with Enhanced Accuracy. *J Magn Reson* **2003**, *161*, 258-264.
- 43. Goddard, T. D.; Huang, C. C.; Meng, E. C.; Pettersen, E. F.; Couch, G. S.; Morris, J. H.; Ferrin, T. E., Ucsf Chimerax: Meeting Modern Challenges in Visualization and Analysis. *Protein Sci* **2018**, *27*, 14-25.
- 44. Zandarashvili, L.; Sahu, D.; Lee, K.; Lee, Y. S.; Singh, P.; Rajarathnam, K.; Iwahara, J., Real-Time Kinetics of High-Mobility Group Box 1 (Hmgb1) Oxidation in Extracellular Fluids Studied by in Situ Protein Nmr Spectroscopy. *J Biol Chem* **2013**, *288*, 11621-11627.
- 45. Sahu, D.; Iwahara, J., Discrete-State Kinetics Model for Nmr-Based Analysis of Protein Translocation on DNA at Equilibrium. *J Phys Chem B* **2017**, *121*, 9548-9556.